

COSMIC VOIDS AND GALAXY BIAS IN THE HALO OCCUPATION FRAMEWORK

JEREMY L. TINKER¹, DAVID H. WEINBERG², & MICHAEL S. WARREN³

Draft version October 1, 2018

ABSTRACT

We investigate the power of void statistics to constrain galaxy bias and the amplitude of dark matter fluctuations. We adopt a Λ CDM cosmological scenario (inflationary cold dark matter with a cosmological constant) and use the halo occupation distribution (HOD) framework to describe the relation between galaxies and dark matter. After choosing HOD parameters that reproduce the mean space density \bar{n}_g and projected correlation function $w_p(r_p)$ measured for galaxy samples with $M_r < -19$ and $M_r < -21$ from the Sloan Digital Sky Survey (SDSS), we predict the void probability function (VPF) and underdensity probability function (UPF) of these samples by populating the halos of a large, high-resolution N-body simulation ($400h^{-1}$ Mpc, 1280^3 particles). If we make the conventional simplifying assumption that the HOD is independent of large scale environment at fixed halo mass, then models constrained to match \bar{n}_g and $w_p(r_p)$ predict nearly identical void statistics, independent of the scatter between halo mass and central galaxy luminosity or statistical uncertainties in HOD parameters. Models with power spectrum normalizations $\sigma_8 = 0.7$ and $\sigma_8 = 0.9$ also predict very similar void statistics, with stronger galaxy bias compensating for weaker dark matter fluctuations in the low- σ_8 model. However, the VPF and UPF are sensitive to environmental variations of the HOD in a regime where these variations have little impact on $w_p(r_p)$. For example, doubling the minimum host halo mass in regions with large scale ($5h^{-1}$ Mpc) density contrast $\delta < -0.65$ has a readily detectable impact on void probabilities of $M_r < -19$ galaxies, and a similar change for $\delta < -0.2$ alters the void probabilities of $M_r < -21$ galaxies at a detectable level. The VPF and UPF provide complementary information about the onset and magnitude of density-dependence in the HOD. By detecting or ruling out HOD changes in low density regions, void statistics can reduce systematic uncertainties in the cosmological constraints derived from HOD modeling, and, more importantly, reveal connections between halo formation history and galaxy properties.

Subject headings: cosmology:theory — large scale structure of the universe

1. INTRODUCTION

VOIDS are an omnipresent feature of the galaxy distribution (Kirshner et al. 1987; de Lapparent, Geller, & Huchra 1991; Vogeley et al. 1994; Hoyle & Vogeley 2004; Conroy et al. 2005; see Rood 1988 for a historical review). Galaxy redshift surveys reveal that underdense regions $30 h^{-1}$ Mpc in diameter are common, and that they can be as large as $50 h^{-1}$ Mpc. A fundamental question regarding the nature of voids is whether they are as empty of matter as they are of light, or whether the breadth and depth of observed voids is a consequence of a lower efficiency of galaxy formation in underdense regions. For the matter distribution, the frequency of large voids is sensitive to departures from Gaussianity in the primordial density fluctuations (Weinberg & Cole 1992). In Gaussian models, the frequency of voids depends on the rms amplitude of matter clustering and on the bias between galaxies and mass (Einasto et al. 1991; Weinberg & Cole 1992; Little & Weinberg 1994). Little & Weinberg (1994) show that void statistics are sensitive not only to the amplitude of galaxy bias, but also to the detailed form of the relation between the underlying matter distribution and galaxy formation efficiency. In this paper, we revisit the connection between voids and galaxy bias in the framework of the halo occupation distribution (HOD), which has emerged in the last few years as a powerful method for characterizing the relationship between

galaxies and mass (Kauffmann et al. 1997; Benson et al. 2000; Seljak 2000; Peacock & Smith 2000; Ma & Fry 2000; Scoccimarro et al. 2001; Berlind & Weinberg 2002, hereafter BW).

Many different methods have been proposed for identifying voids and quantifying their importance (Ryden & Turner 1984; Kauffmann & Fairall 1991; Kauffmann & Melott 1992; El-Ad & Piran 1997; Hoyle & Vogeley 2002). In this paper we will use two of the simplest statistical measures of cosmic voids: the void probability function (VPF, denoted P_0) and the underdensity probability function (UPF, denoted P_U). The VPF is defined as the probability that a randomly placed sphere of radius r contains no galaxies of a given class. The UPF is similar but quantifies the probability that the galaxy density within a randomly placed sphere is less than a defined threshold, usually 0.2 times the mean density for galaxies of that type. The VPF depends on the full hierarchy of n -point correlation functions (White 1979), so in principle it contains complementary information to the two-point correlation function $\xi_g(r)$. The first significant measurement of the VPF and UPF was the analysis of the CfA redshift survey by Vogeley et al. (1992, 1994). The current state of the art is the analysis of the Two-Degree Field Galaxy Redshift Survey (2dFGRS, Colless et al. 2001) by Hoyle & Vogeley (2004), which covered 1500 deg^2 to a median redshift of ~ 0.1 . Forthcoming results for the Sloan Digital Sky Survey (SDSS, York et al. 2000) should yield even more precise measurements of the void distribution owing to its larger survey volume, which will ultimately extend over nearly a quarter of the sky.

The galaxies that define the voids are, in general, a biased tracer of the underlying mass distribution. A fully non-

¹ Kavli Institute for Cosmological Physics, Department of Astronomy & Astrophysics, The University of Chicago, IL 60637

² Department of Astronomy, The Ohio State University, 140 W. 18th Avenue, Columbus, Ohio 43210

³ Theoretical Astrophysics, Los Alamos National Laboratories, P.O. Box 1663, Los Alamos, New Mexico, 87545

linear model of galaxy bias is required to compare theory to observations for any clustering measure. The HOD formalism describes bias at the level of dark matter “halos,” where a halo is a structure of overdensity $\rho/\bar{\rho} \sim 200$, in approximate dynamical equilibrium (identified in this paper by the Friends-of-Friends algorithm, see §2). With this definition, the mass function, spatial clustering, and velocity statistics of dark matter halos are essentially independent of gas physics, and they can be determined accurately for a given cosmology using high-resolution N-body simulations (e.g., Warren et al. 2005; Springel et al. 2005) or analytic approximations calibrated on these simulations. In the HOD framework, one specifies the bias of any particular class of galaxies by specifying $P(N|M)$, the probability that a halo of mass M houses N such galaxies, together with any spatial or velocity biases between galaxies and dark matter *within* individual halos. To the extent that the HOD is independent of a halo’s larger scale environment (a point that we return to below), this description of bias is complete, for all clustering statistics on all scales. The HOD framework has been used to model measurements of the projected galaxy correlation function, $w_p(r_p)$, from the SDSS (Zehavi et al. 2004a, 2005; Tinker et al. 2005a). The conditional luminosity function, which combines the HOD with luminosity information, has been used to analyze the correlation function and luminosity function of the Two-Degree Field Galaxy Redshift Survey (e.g. Yang et al. 2002, 2004; van den Bosch et al. 2003). Approaches to modeling void statistics with the HOD have been discussed by Benson (2001) and BW. Here we follow the approach of BW and calculate the VPF and UPF by populating dark matter halos identified in collisionless N-body simulations.

It is well known that the halo mass function correlates with large-scale environment (Bond et al. 1991; Lemson & Kauffmann 1999; Sheth & Tormen 2002). Massive halos form from high-sigma fluctuations in the primordial density field, which reside preferentially in regions that are overdense on larger scales (Kaiser 1984). In low-density regions, high-sigma fluctuations are rare, so these environments are dominated by low-mass halos. We therefore expect void statistics to be sensitive to halo occupation at low halo masses, where the occupation number is zero or one. BW adopted a power-law mean occupation function for galaxies above a luminosity threshold, i.e., $\langle N \rangle_M \equiv \sum NP(N|M) = (M/M_1)^\alpha$, with a cutoff at M_{\min} below which halos could not house galaxies above the threshold. Their results showed a strong correlation between M_{\min} and the sizes of voids. Here we adopt a more physically motivated occupation function that divides halo occupation into central and satellite galaxies (Guzik & Seljak 2002; Kravtsov et al. 2004; Zheng et al. 2005). In this parameterization, the behavior of $\langle N \rangle_M$ at low masses is essentially determined by the relation between halo mass and the properties of the central galaxy. For each galaxy population that we model, we only consider HOD models that are constrained to match the mean space density \bar{n}_g and the projected correlation function $w_p(r_p)$ of SDSS galaxies measured by Zehavi et al. (2005). In this respect, we are investigating what *additional* information can be obtained from void statistics once these constraints have been imposed. In this context, we want to answer several questions:

1. Do void statistics provide additional information on the minimum halo mass for a galaxy sample, within the range allowed by the constraints of matching the observed \bar{n}_g and $w_p(r_p)$?

2. Are void statistics sensitive to the scatter in the relation between halo mass and central galaxy luminosity, which alters the *form* of the cutoff in $\langle N \rangle_M$?

3. Can void statistics discriminate among values of σ_8 , the rms linear theory amplitude of *mass* fluctuations in $8 h^{-1}$ Mpc spheres, if *galaxy* HODs are chosen to reproduce the observed correlation function? (Here $h \equiv H_0/100 \text{ km s}^{-1} \text{ Mpc}^{-1}$.)

We will show that the answer to all three questions is, for practical purposes, no. Once one has matched \bar{n}_g and $w_p(r_p)$, variations in the VPF and UPF that result from varying M_{\min} within the allowed range, from changing the form of the low-mass cutoff, or from altering σ_8 , are all at the level of error expected from the full SDSS sample. We will demonstrate that the aspect of the HOD that has the greatest influence on void statistics is the fraction of galaxies that are satellites, because once this is determined the cutoff mass M_{\min} is essentially fixed by \bar{n}_g . The satellite fraction is well constrained by matching $w_p(r_p)$. Therefore, within the standard cosmological and HOD framework, the predicted void statistics are remarkably robust. The imposition of the observed correlation function as a constraint is the crucial difference between our work and the analysis of BW, and it accounts for our differing conclusions about the information content of void statistics.

In the standard implementation of HOD models, including those that lead to the conclusions mentioned above, the statistics of galaxy occupation are assumed to depend on a halo’s mass, independent of its larger scale environment. Semi-analytical models of galaxy formation that incorporate this assumption reproduce the observed correlations of galaxy luminosity, color, and morphology with environment (Benson et al. 2003; Norberg et al. 2001); these arise because the halo mass function itself varies with large scale overdensity. Direct observational support for this assumption comes from the work of Blanton et al. (2004), who show that the variation of blue galaxy fraction with overdensity measured on a $6 h^{-1}$ Mpc scale is fully explained by the variation on the $1 h^{-1}$ Mpc scale characteristic of individual large halos. On the theoretical side, Bond et al.’s (1991) excursion set derivation of the extended Press-Schechter (1974) formalism predicts that halo formation histories at fixed mass are independent of large scale overdensity (White (1996)), while Berlind et al. (2003) show that the HOD for a baryon-mass selected sample from Weinberg et al.’s (2004) smoothed particle hydrodynamic simulation has no detectable dependence on environment. However, while early N-body investigations (Lemson & Kauffmann 1999; Sheth & Tormen 2004) showed little or no correlation between halo formation histories and environment for masses above $M \sim 10^{13} h^{-1} M_\odot$, several recent studies (Gao et al. 2005; Harker et al. 2005; Wechsler et al. 2005; Zhu et al. 2006) show much stronger correlations at lower masses. The correlation of halo formation time with large scale overdensity, which is especially prominent in the mass range $M \sim 10^{11} h^{-1} M_\odot$ of individual dwarf galaxy halos, raises the possibility that the galaxy HOD itself varies with halo environment, at least in the single-galaxy regime.

Void statistics should be a sensitive probe of any such environmental variations, since they characterize extreme environments and are not washed out by the strong signals from multiple galaxy halos. In §4, we investigate a simple class of extended HOD models in which the minimum host mass M_{\min} changes by a fixed factor in low density environments. The VPF and UPF prove quite sensitive to such changes, and the two statistics provide somewhat complementary information

about the density dependence of M_{\min} . By tightly constraining this dependence, void statistics can test fundamental ideas about galaxy formation and provide essential input to cosmological applications of HOD methods (Zheng & Weinberg 2005).

2. NUMERICAL SIMULATIONS AND HOD MODELS

The simulation used in this paper was performed using the Hashed Oct-Tree code of Warren & Salmon (1993), and is similar to those presented in Seljak & Warren (2004) and Warren et al. (2005). This simulation is substantially larger in terms of particle number, with 1280^3 particles. The simulation box is $400 h^{-1} \text{Mpc}$ per side, giving a mass resolution of $2.5 \times 10^9 h^{-1} M_{\odot}$. Halos are identified in the simulation by the friends-of-friends technique (Davis et al. 1985) with a linking length 0.2 times the mean interparticle separation. For low-luminosity, $M_r \sim -19$ galaxies, the minimum mass halo roughly corresponds to a 100-particle halo. The linear power spectrum used to create the initial conditions was calculated with CMBFAST (Seljak & Zaldarriaga 1996), with the parameter set $(\Omega_m, \Lambda, \sigma_8, h, \Omega_b) = (0.3, 0.7, 0.9, 0.7, 0.04)$ and a scale-invariant inflationary power spectrum. We use the output at $z = 0.459$, where the linear growthfactor is 0.79, to represent a universe with $\sigma_8 = 0.7$, scaling the peculiar velocities and internal dispersions of halos to values appropriate for $\Omega_m = 0.3$ (see Tinker et al. [2005b] and Zheng et al. [2002] for a discussion of this technique).

This simulation is ideal for our purposes because of its high mass resolution and large box size. High mass resolution is required to model low-luminosity galaxy populations. The lowest luminosity SDSS sample that we can model is $M_r < -19$.⁴ The statistical errors in measuring void statistics are dominated by the finite number of independent volumes in the simulation (or survey), once the voids become large. The $(400 h^{-1} \text{Mpc})^3$ simulation volume is comparable to that of the volume-limited sample of bright $M_r < -21$ galaxies expected for the full SDSS. Therefore, the statistical errors in our calculations are comparable to those expected from the SDSS analysis. The volume of the full SDSS $M_r < -19$ sample will be approximately the same as one octant of our simulation, and our errors are therefore smaller by $\sim \sqrt{8}$. In practice, the observational errors will be somewhat larger than the error in periodic cubes of the same volume because edges and ‘‘holes’’ in the survey region mean that one cannot use the full volume for void measurements.

To determine HOD parameters, we use the measurements of $w_p(r_p)$ from Zehavi et al. (2005) for galaxies brighter than $M_r = -21$ and $M_r = -19$. We choose these two samples because they probe different regimes of the halo mass function; bright galaxies preferentially occupy high-mass halos, while the majority of lower luminosity galaxies occupy lower mass halos (Zehavi et al. 2005). We use the five-parameter HOD model of Zheng et al. (2005), which is flexible enough to precisely describe the halo occupation functions predicted from semi-analytic galaxy formation models and hydrodynamic simulations. The full mean occupation function is the sum of the average number of central galaxies and satellite galaxies in halos of mass M , i.e. $\langle N \rangle_M = \langle N_{\text{sat}} \rangle_M + \langle N_{\text{cen}} \rangle_M$. For satellite galaxies, the mean occupation is

$$\langle N_{\text{sat}} \rangle_M = \left(\frac{M - M_{\text{cut}}}{M_1} \right)^\alpha, \quad (1)$$

where M is the halo mass, M_{cut} is a cutoff mass below which a halo cannot host a satellite galaxy, $M_1 + M_{\text{cut}}$ is the mass at which a halo hosts one satellite on average, and α is the power-law exponent of the relation, a number usually near one. The distribution of satellite galaxies about the mean is assumed to be Poisson, i.e. $\langle N_{\text{sat}}(N_{\text{sat}} - 1) \rangle = \langle N_{\text{sat}} \rangle^2$. This assumption is well-motivated by both collisionless and hydrodynamic studies of halo substructure (Kravtsov et al. 2004; Zheng et al. 2005), and by observational studies of galaxies within clusters (Lin et al. 2004).

For central galaxies, the HOD of Zheng et al. (2005) contains a soft transition between one and zero galaxies,

$$\langle N_{\text{cen}} \rangle_M = \frac{1}{2} \left[1 + \text{erf} \left(\frac{\log M - \log M_{\min}}{\sigma_{\log M}} \right) \right], \quad (2)$$

where $\text{erf}(x)$ is the error function, M_{\min} is characteristic minimum mass, and $\sigma_{\log M}$ is a transition width. As defined in equation (2), M_{\min} is the mass at which $\langle N_{\text{cen}} \rangle_M = 0.5$. All logarithms are base ten. As $\sigma_{\log M}$ approaches zero, equation (2) approaches a step function at M_{\min} . Since the number of central galaxies is assumed to be zero or one by definition, the distribution of N_{cen} about $\langle N_{\text{cen}} \rangle_M$ is a nearest-integer distribution (a.k.a. Bernoulli distribution).

For full details regarding the calculation of $w_p(r_p)$ for a given cosmology and HOD, we refer the interested reader to Zheng (2004) and Tinker et al. (2005a) and the references therein. In the analysis of this paper, we have used the approach described in Tinker et al. (2005a) with one modification; the parameters of the halo bias function listed in Appendix A ($a = 0.707$, $b = 0.35$ and $c = 0.8$) have been changed to better match those of the simulation we will be using to calculate P_0 : a and b are the same, but $b = 0.28$, which lowers the bias of low-mass halos by about 5%. (The jackknife errors in the bias of low-mass halos in the simulation are themselves $\sim 5\%$, so we are not claiming that this value should be adopted universally.) The purpose of our HOD modeling is to find HOD parameters to populate our simulation. It would make little sense to make mock galaxy populations that do not match the analytic model or, more importantly, the SDSS observations.

We assume $\Omega_m = 0.3$ throughout this paper. For a fixed linear matter power spectrum, the choice of Ω_m has little influence on the mass function and clustering of dark matter halos (Zheng et al. 2002) and therefore has minimal influence on these calculations. The shape of $P_{\text{lin}}(k)$ is well constrained empirically by the combination of microwave background anisotropies and large-scale galaxy clustering measurements (e.g., Percival et al. 2002; Spergel et al. 2003; Tegmark et al. 2004a). On a more practical level, we are required to match the linear matter power spectrum used to create the initial conditions of the simulation, so all calculations use the CMBFAST power spectrum with the parameters listed in §2.1. This $P_{\text{lin}}(k)$ is in good agreement with the aforementioned observations, though the recent analysis of Sanchez et al. (2005) favors a spectrum with somewhat more large scale power.

For a given galaxy sample, the HOD parameters are determined through χ^2 minimization using the full covariance matrix estimated through jackknife resampling of the observational sample (see Zehavi et al. 2005). The number of free parameters in equations (1) and (2) is five, but it is reduced

⁴ All absolute magnitudes are quoted for $h = 1$ throughout the paper. For other values, one should add $5 \log h$.

TABLE 1
HOD PARAMETERS FOR MODELS IN FIGURE 3

M_r	σ_8	$\sigma_{\log M}$	$\log M_{\min}$	$\log M_1$	α	$\log M_{\text{cut}}$
-19	0.9	0.1	11.54	12.83	1.019	11.38
-19	0.9	0.6	11.70	12.84	1.018	12.37
-19	0.7	0.1	11.52	12.69	1.020	12.45
-21	0.9	0.1	12.68	13.89	1.063	12.25
-21	0.9	0.6	12.86	13.89	1.071	13.24
-21	0.7	0.1	12.64	13.69	1.107	13.28

NOTE. — All masses are in units of $h^{-1} M_{\odot}$.

to four by fixing M_{\min} in order to match the observed space density of galaxies. To populate the halos, central galaxies are placed at the center of mass of each halo, while satellite galaxies are placed randomly about the center of mass assuming a Navarro, Frenk, & White (1997) density profile appropriate for the halo’s mass using the parameterization of Bullock et al. (2001). This technique places the galaxies in a spherically symmetric distribution about the central galaxy, an assumption which has negligible importance in the context of this work because we are most interested in halos that host only central galaxies.

3. CONNECTING VOIDS AND $w_p(r_p)$ WITH THE HOD

3.1. Variations in the Minimum Mass Scale

The results of BW demonstrated that the VPF is highly sensitive to the minimum mass scale, and mostly insensitive to the amplitude and slope of the occupation function, implying that M_{\min} can be constrained by measurements of void statistics. We test this implication with two significant improvements over the analysis of BW: our central-satellite approach to the occupation function, as described in §2, and a full statistical comparison of a given HOD model with $w_p(r_p)$ data.

To quantify the range of M_{\min} allowed by the observed $w_p(r_p)$, we first determine the best-fit values of the HOD parameters, including M_{\min} , for both the $M_r < -19$ and $M_r < -21$ samples with $\sigma_{\log M}$ fixed at 0.1. This value of $\sigma_{\log M}$ creates an occupation function with a fairly sharp central cutoff, but the strength of the inferred constraints on M_{\min} will be consistent for any reasonable value of $\sigma_{\log M}$. We keep $\sigma_{\log M}$ fixed to isolate the effect of changing the minimum mass scale only, without any change in the shape of the central cutoff. The two parameters that control $\langle N_{\text{cen}} \rangle_M$ have quite different physical interpretations, so we examine their effect on $w_p(r_p)$ and void statistics separately. The best-fit values of the HOD parameters for $\sigma_{\log M} = 0.1$ are listed in Table 1. For $M_r < -19$ galaxies, we find $M_{\min} = 3.60 \times 10^{11} h^{-1} M_{\odot}$, while for the brighter $M_r < -21$ galaxies, we find $M_{\min} = 4.78 \times 10^{12} h^{-1} M_{\odot}$. For all calculations, we assume $\sigma_8 = 0.9$.

Figure 1 demonstrates that the allowed range of M_{\min} is quite narrow. Panels (a) and (b) plot $\Delta\chi^2$ for models in which M_{\min} is varied around the minimum value for the faint and bright galaxy samples, respectively. As M_{\min} is varied, the best-fit HOD parameters are determined once again by χ^2 minimization, but with M_{\min} and $\sigma_{\log M}$ held constant and M_1 fixed by the space density. This leaves two free parameters, α and M_{cut} , for the χ^2 analysis. For $M_r < -19$ galaxies, $\Delta \log M_{\min} = \pm 0.05$ produces $\Delta\chi^2 = 6$. The constraints for the $M_r < -21$ sample are even narrower, with $\Delta \log M_{\min} = \pm 0.015$ producing $\Delta\chi^2 = 6$. The change in χ^2

is symmetric about the minimum for both magnitude thresholds. The tighter constraints on M_{\min} for $M_r < -21$ are mostly a result of smaller observational errors for this sample.

The tight constraints on M_{\min} are a result of the information $w_p(r_p)$ reveals about the fraction of galaxies that are satellites. The fraction of satellites f_{sat} influences the shape and amplitude of the correlation function at small scales, where pairs from within a single halo dominate. Once the satellite fraction is known, the value of M_{\min} (for a given $\sigma_{\log M}$) is determined by the number density constraint. Figures 1c and 1d plot the model $w_p(r_p)$ functions for the two values of M_{\min} that yield $\Delta\chi^2 = 6$ in the upper panels (3.2×10^{11} and $4.0 \times 10^{11} h^{-1} M_{\odot}$ for $M_r < -19$, and 4.7×10^{12} and $5.1 \times 10^{12} h^{-1} M_{\odot}$ for $M_r < -21$). HOD calculations for the high and low M_{\min} are shown with the solid and dotted lines, respectively, while points with error bars are the SDSS data. As M_{\min} increases, f_{sat} increases in order to preserve the space density of galaxies, steepening and amplifying the one-halo term of the correlation function. This behavior is most easily seen in the $M_r < -21$ models in panel (d). The model $w_p(r_p)$ curves are consistent with each other and with the data until $r \lesssim 1 h^{-1} \text{Mpc}$, which represents the transition scale between the one-halo term and the two-halo term. Below this scale the curves diverge, with the high- M_{\min} curve above the low- M_{\min} curve.

The behavior for the $M_r < -19$ models in panel (c) is a bit different: the high- M_{\min} model has a steeper slope in the one-halo regime, but its amplitude is lower except at very small scales. In this case, the adjustment of α and M_{cut} after changing M_{\min} provides enough freedom to lower the one-halo contribution to $w_p(r_p)$. If we keep these parameters fixed in addition to $\sigma_{\log M}$ and the (changed) value of M_{\min} , we obtain the dashed curve in Figure 1c, which lies well above the data all scales.

Figure 2 shows the void statistics for the high- and low- M_{\min} models of Figure 1. The VPF is calculated for each galaxy distribution by randomly placing 10^6 spheres of radius r within the box and counting the fraction that are empty. The UPF is calculated in the same manner as the VPF, but each sphere which has a mean interior density less than 0.2 times the mean galaxy density is counted. The error at each r is determined from the jackknife method, dividing the simulation volume into octants. Alternatively, Hoyle & Vogeley (2004) estimate observational errors from the error in the mean of void counts expected if these follow a binomial distribution:

$$\sigma(P_0) = \frac{(P_0 - P_0^2)^{1/2}}{N_{\text{ind}}^{1/2}}, \quad (3)$$

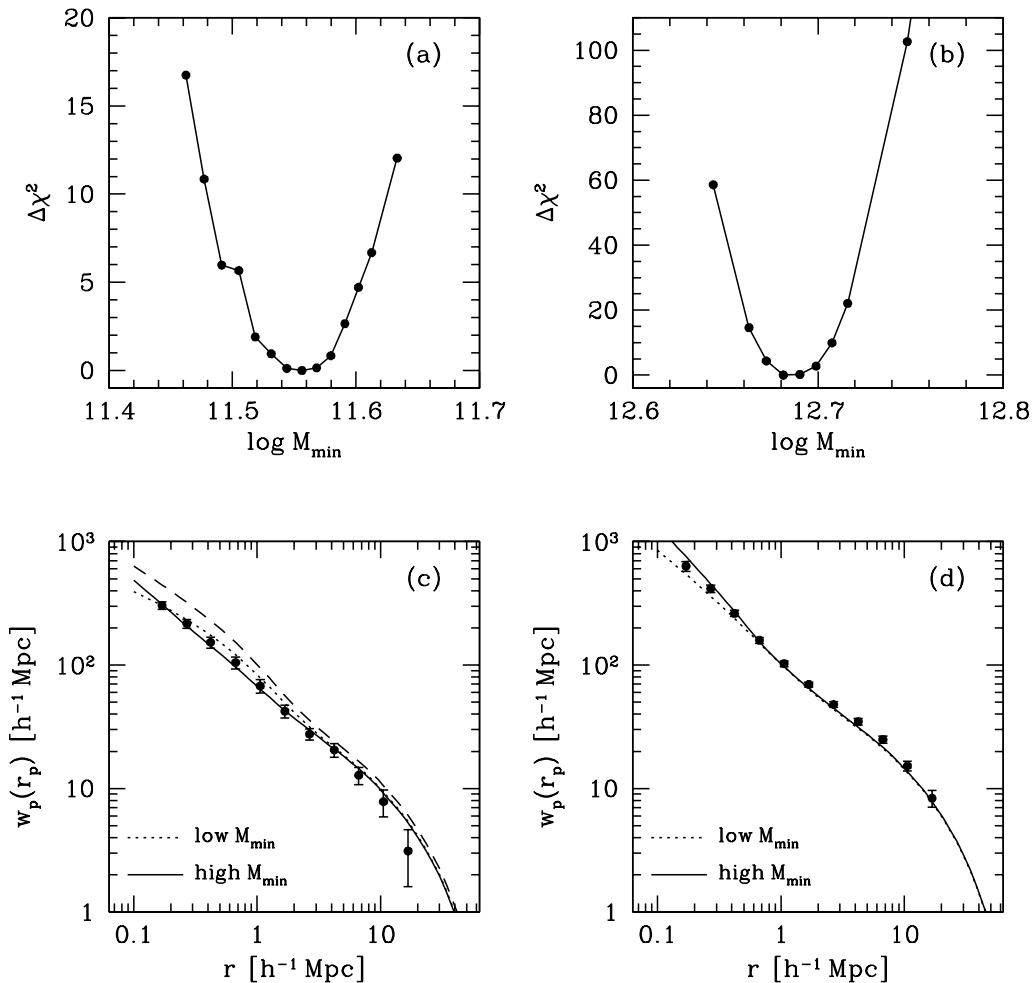


FIG. 1.— Panel (a): $\Delta\chi^2$ of HOD models as a function of M_{\min} with respect to the $M_r < -19$ $w_p(r_p)$ data. All models have $\sigma_{\log M} = 0.1$, but the parameters that determine $\langle N_{\text{sat}} \rangle_M$ are left free to match the data. Panel (b): Same as (a), but for $M_r < -21$ galaxies. Panel (c): Best-fit HOD models for $M_r < -19$ for the highest and lowest values of M_{\min} with $\Delta\chi^2 \approx 6$ from panel (a). The solid line is $M_{\min} = 4.0 \times 10^{11} h^{-1} M_{\odot}$, and the dotted line is $M_{\min} = 3.2 \times 10^{11} h^{-1} M_{\odot}$. The dashed line represents the high- M_{\min} model with the parameters of $\langle N_{\text{sat}} \rangle_M$ taken from the best-fit model from Table 1. Panel (d): Same as (c), but for $M_r < -21$. The solid line is $M_{\min} = 5.1 \times 10^{12} h^{-1} M_{\odot}$, and the dotted lines is $M_{\min} = 4.7 \times 10^{12} h^{-1} M_{\odot}$.

where $N_{\text{ind.}} = 3R_{\text{box}}^3/(4\pi r^3)$ is the number of independent volumes in the box at each r for which P_0 is calculated. For the VPF, the jackknife errors are consistent with those determined from equation (3) at radii where $P_0(r) \approx 0.01$, while at larger radii the jackknife errors are smaller by a factor of two or more. At smaller radii, the jackknife errors are significantly larger, but the percentage errors are still less than 1%. All calculations are done in redshift space using the distant observer approximation, allowing us to use one axis of the box as the observer’s line of sight and impose periodic boundaries for our galaxies shifted past the edge of the cube. We find little difference between the void statistics calculated in and real and redshift space, as also noted by Little & Weinberg (1994).

For the high space density, $M_r < -19$ sample, the predicted VPF falls rapidly, dropping to $P_0(r) = 10^{-3}$ at $r = 11 h^{-1} \text{Mpc}$ (Figure 2a). As expected, the low- M_{\min} model has a lower VPF at all radii, but because the range in M_{\min} allowed by the $w_p(r_p)$ and \bar{n}_g constraints is so small, the difference between the low- and high- M_{\min} models is small. Since our errors bars for this simulated sample should be smaller than those for the

full SDSS, the difference is likely to be indiscernible in practice. Note that errors at different r are highly correlated, as any large void would also contain smaller empty spheres, so the points do not scatter about a smooth curve by the amount of their error bars. For the $M_r < -21$ sample, voids are larger, with $P_0(r) = 10^{-3}$ at $r = 20 h^{-1} \text{Mpc}$ (Figure 2b). The tight constraints on M_{\min} for this sample lead to a very small difference between the low- and high- M_{\min} VPFs, again smaller than the expected SDSS errors.

The VPFs for the faint and bright samples are shown in Figures 2c and 2d, respectively. It is more likely to find a region with low density contrast than a completely empty region, so $P_U \geq P_0$ at all r . The VPF is also not as steep a function of r , since the $n_g \leq 0.2\bar{n}_g$ threshold allows a larger number of galaxies in larger radius spheres. The results for the VPF parallel the results of the VPF; there is a small difference in the low- and high- M_{\min} models, with high- M_{\min} producing higher P_U , but the difference between the models is only marginally significant.

BW reached different conclusions about the sensitivity of

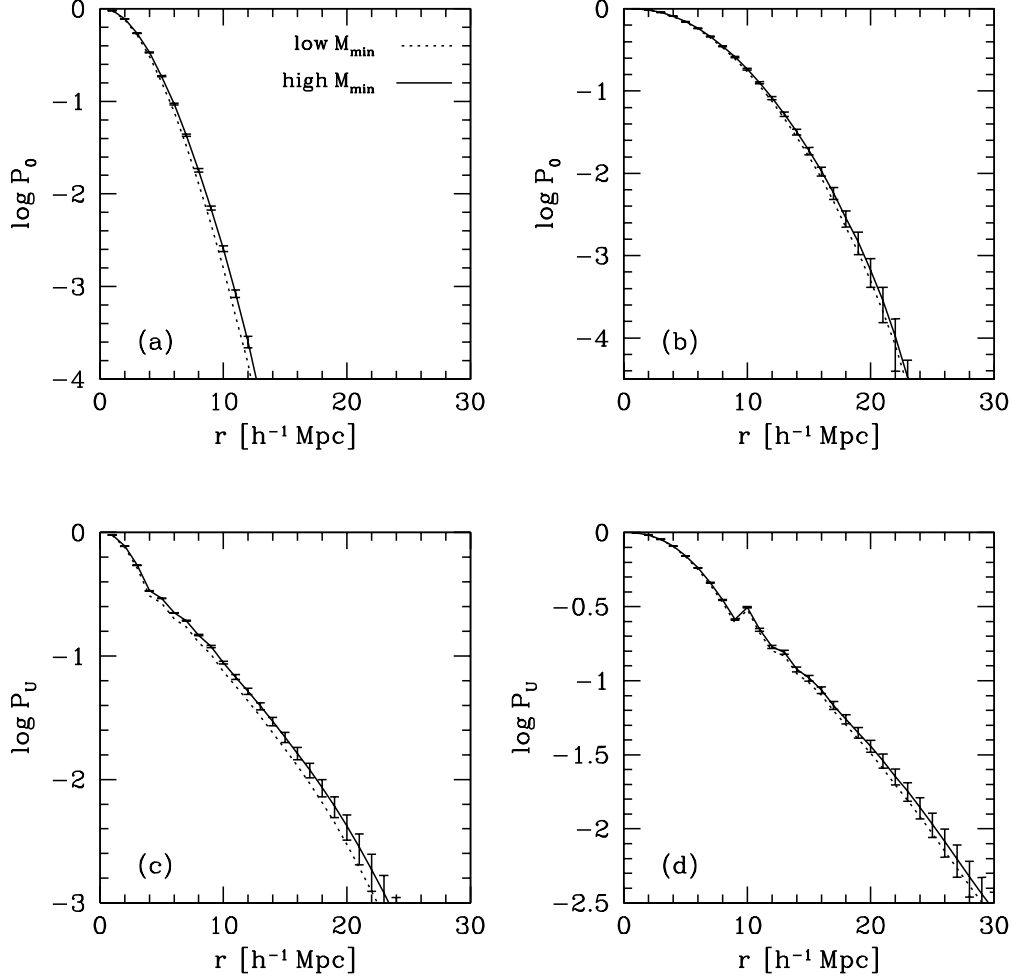


FIG. 2.— Panel (a): Void probability function (VPF) for the high- and low- M_{\min} models of Figure 1c for the $M_r < -19$ galaxy sample. Panel (b): Same as (a), but for the $M_r < -21$ sample from Figure 1d. Panel (c): Underdense probability distribution (UPF) for the high- and low- M_{\min} models of the $M_r < -19$ sample. Panel (d): Same as (c), but for $M_r < -21$ galaxies.

the VPF to M_{\min} because they did not impose $w_p(r_p)$ as a constraint. They varied M_{\min} by a factor of 8, producing radical changes in the VPF, but also changing the correlation function. The VPF is sensitive to M_{\min} , but Figures 1 and 2 show that $w_p(r_p)$ constrains M_{\min} tightly enough that void statistics cannot add much further leverage. This result was also found by Conroy et al. (2005) in their analysis of voids in the DEEP2 and SDSS surveys. The constraints on M_{\min} in Figure 1 will become tighter as the full sample of SDSS galaxies is analyzed, significantly reducing the errors on $w_p(r_p)$.

3.2. Variations in σ_8 and the Central Cutoff

The shape of the central galaxy cutoff reflects the scatter between galaxy properties and host halo mass. A soft cutoff corresponds to significant scatter, allowing some halos with $M \ll M_{\min}$ to host a galaxy within the sample and some halos with $M > M_{\min}$ to be scattered out of the sample. In the context of our luminosity-threshold samples the scatter is between luminosity and mass, but it can be reflected in any quantity used to define the sample, such as surface brightness, color, or nuclear activity.

The shape of the central cutoff may alter void statistics be-

cause the halos that outline the voids are low mass. Numerical simulations of void regions show that the maximum halo mass within voids increases from the center of the void to its outer edge (Gottlöber et al. 2003). Allowing some galaxies to occupy halos below M_{\min} could effectively “shrink” the voids. To quantify the effect of the shape of $\langle N_{\text{cen}} \rangle_M$, we fix $\sigma_{\log M}$ at six values ranging evenly from 0.1 to 0.6. At $\sigma_{\log M} = 0.1$, $\langle N_{\text{cen}} \rangle_M$ is nearly a step function at M_{\min} , while for $\sigma_{\log M} = 0.6$ the probability of finding a galaxy in a halo of mass $M_{\min}/10$ is still $\sim 1\%$, which can be significant given the steepness of the halo mass function. For each value of $\sigma_{\log M}$, we find the best-fit values of the four remaining HOD parameters by χ^2 minimization.

We also investigate the influence of the dark matter clustering amplitude by considering a model with $\sigma_{\log M} = 0.1$ but $\sigma_8 = 0.7$. Power spectra with lower amplitudes produce smaller voids in the matter distribution, but the effect on galaxy voids is not immediately clear. A model with lower σ_8 must have higher galaxy bias to match $w_p(r_p)$. This requires shifting more galaxies into higher mass halos, and thus out of low-density regions.

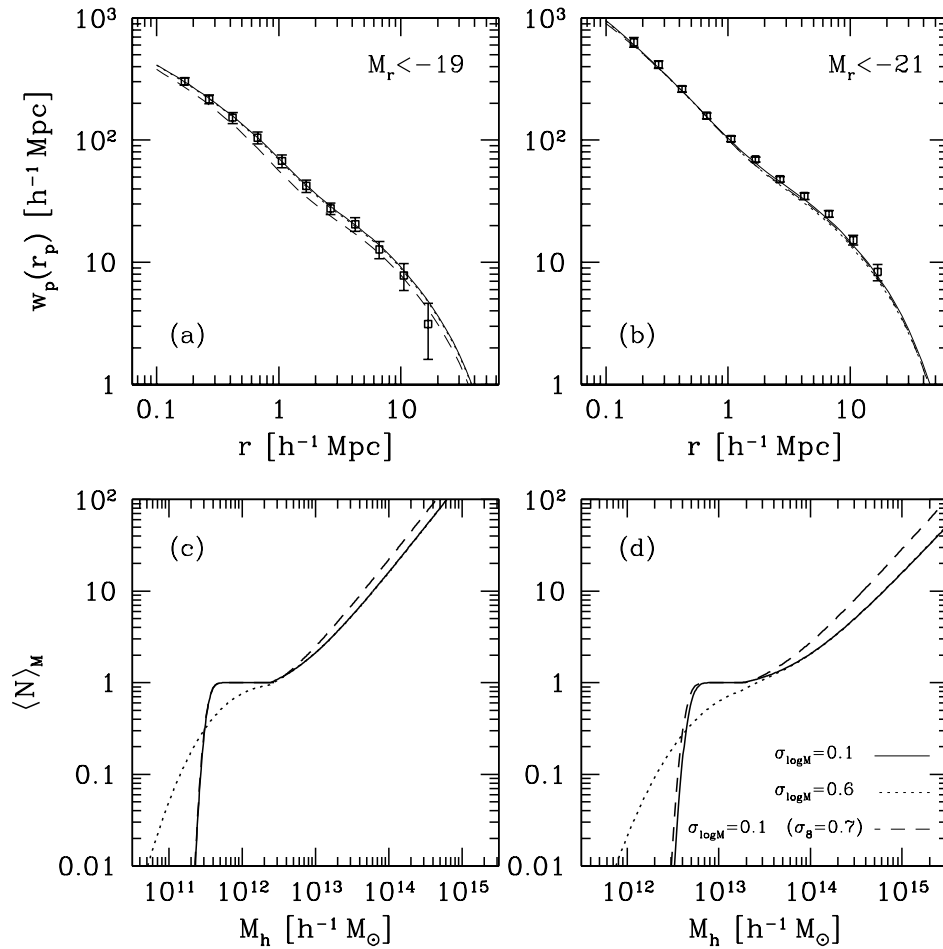


FIG. 3.— HOD fits to SDSS samples for $M_r < -19$ (left panels) and $M_r < -21$ (right panels). Panels (a) and (b): Projected correlation functions. Points with error bars are SDSS data. Lines represent HOD models (see legend in panel d). Panels (c) and (d): Halo occupation functions derived from the data. The x -axis is halo mass and the y -axis is the average number of galaxies.

Figure 3a plots $w_p(r_p)$ for the data for $M_r < -19$ and for three of the HOD models: $(\sigma_8, \sigma_{\log M}) = (0.9, 0.1)$, $(0.9, 0.6)$, and $(0.7, 0.1)$. The two models with higher σ_8 are excellent fits to the observations and are nearly indistinguishable both visually and in χ^2 . Panel (c) plots $\langle N \rangle_M$ against M for these three models. Increasing $\sigma_{\log M}$ produces virtually identical correlation functions because the bias function of halos below $\sim 10^{12} h^{-1} M_\odot$, where the differences in $\langle N \rangle_M$ begin, is relatively flat. Redistributing galaxies from halos of $2 \times 10^{12} h^{-1} M_\odot$ into lower mass halos near $10^{11} h^{-1} M_\odot$ does not significantly change the large scale galaxy bias factor (0.94 and 0.93 for $\sigma_{\log M} = 0.1, 0.6$). The large-scale clustering is thus unchanged. The differences in $\langle N_{\text{sat}} \rangle_M$ are minimal, so the one-halo term is also unaltered. The only change in $w_p(r_p)$ from $\sigma_{\log M} = 0.1$ to 0.6 is in the two-halo term at small scales, $r \lesssim 0.8 h^{-1} \text{Mpc}$, but at these scales $w_p(r_p)$ is dominated by the one-halo term and the changes cannot be distinguished. The fit for the $\sigma_8 = 0.7$ model does not match the data as well and has a $\Delta\chi^2$ of approximately five relative to the $\sigma_8 = 0.9$ fits. The low amplitude of matter clustering for this model can only be partially overcome by creating an occupation function

that has more galaxies in high-mass halos. Changes to $\sigma_{\log M}$ make little difference in the agreement.

Figure 3b shows the HOD fits to the $M_r < -21$ sample for the same three models. All three appear nearly equivalent, but statistically, the $(\sigma_8, \sigma_{\log M}) = (0.9, 0.1)$ model has $\chi^2 = 5.5$, while the $(0.9, 0.6)$ model has $\chi^2 = 11.4$ and $(0.7, 0.1)$ has $\chi^2 = 10.0$. For both values of σ_8 , the χ^2 of the HOD fit increases monotonically with $\sigma_{\log M}$. In contrast to the $M_r < -19$ sample, moving galaxies from $10^{13} h^{-1} M_\odot$ halos into smaller ones has a noticeable effect on the average halo bias of the sample (the galaxy bias is 1.20 and 1.15 for $\sigma_{\log M} = 0.1$ and 0.6 respectively). The subsequent HOD model is less able to match the observed amplitude of galaxy clustering.

Figure 4 shows the values of f_{sat} determined from the best-fit HOD parameters as a function of $\sigma_{\log M}$, for $\sigma_8 = 0.9$. For the $M_r < -19$ sample, f_{sat} for all models is approximately 0.23, with only modest variation around this mean. For $M_r < -21$ galaxies, $f_{\text{sat}} \approx 0.15$ for all $\sigma_{\log M}$ values. For higher $\sigma_{\log M}$, the best-fit M_{min} is also higher to compensate for the additional number of central galaxies occupying $M < M_{\text{min}}$ halos. But regardless of the shape of $\langle N_{\text{cen}} \rangle_M$, the correlation

TABLE 2
PREDICTED VOID STATISTICS FOR $M_r < -19$
GALAXIES

r [h^{-1} Mpc]	$P_0(r)$	$P_U(r)$
1	$(9.50 \pm 0.01) \times 10^{-1}$	$(9.50 \pm 0.00) \times 10^{-1}$
2	$(7.62 \pm 0.02) \times 10^{-1}$	$(7.61 \pm 0.02) \times 10^{-1}$
3	$(5.21 \pm 0.02) \times 10^{-1}$	$(5.21 \pm 0.03) \times 10^{-1}$
4	$(3.12 \pm 0.03) \times 10^{-1}$	$(3.12 \pm 0.03) \times 10^{-1}$
5	$(1.67 \pm 0.02) \times 10^{-1}$	$(2.75 \pm 0.03) \times 10^{-1}$
6	$(7.95 \pm 0.19) \times 10^{-2}$	$(2.07 \pm 0.03) \times 10^{-1}$
7	$(3.51 \pm 0.12) \times 10^{-2}$	$(1.79 \pm 0.03) \times 10^{-1}$
8	$(1.39 \pm 0.07) \times 10^{-2}$	$(1.35 \pm 0.03) \times 10^{-1}$
9	$(5.10 \pm 0.35) \times 10^{-3}$	$(1.08 \pm 0.03) \times 10^{-1}$
10	$(1.78 \pm 0.20) \times 10^{-3}$	$(7.92 \pm 0.33) \times 10^{-2}$
11	$(5.44 \pm 0.77) \times 10^{-4}$	$(6.14 \pm 0.31) \times 10^{-2}$
12	$(1.51 \pm 0.36) \times 10^{-4}$	$(4.68 \pm 0.29) \times 10^{-2}$
13	$(2.60 \pm 0.95) \times 10^{-5}$	$(3.53 \pm 0.26) \times 10^{-2}$
14	$(1.00 \pm 1.00) \times 10^{-7}$	$(2.64 \pm 0.24) \times 10^{-2}$
15	—	$(1.96 \pm 0.21) \times 10^{-2}$
16	—	$(1.44 \pm 0.19) \times 10^{-2}$
17	—	$(1.05 \pm 0.16) \times 10^{-2}$
18	—	$(7.49 \pm 1.38) \times 10^{-3}$
19	—	$(5.24 \pm 1.17) \times 10^{-3}$
20	—	$(3.56 \pm 0.97) \times 10^{-3}$
21	—	$(2.38 \pm 0.78) \times 10^{-3}$
22	—	$(1.57 \pm 0.62) \times 10^{-3}$
23	—	$(1.01 \pm 0.47) \times 10^{-3}$
24	—	$(6.31 \pm 3.51) \times 10^{-4}$
25	—	$(3.85 \pm 2.53) \times 10^{-4}$

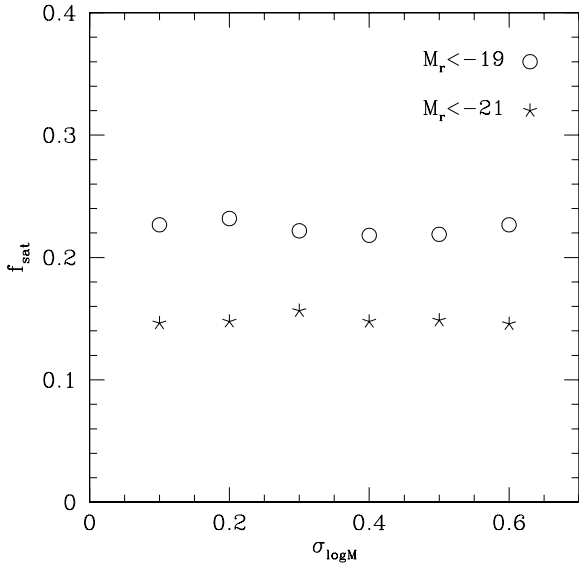


FIG. 4.— Fraction of galaxies that are satellites, f_{sat} , as a function of $\sigma_{\log M}$ for both $M_r < -19$ and $M_r < -21$ galaxies.

function drives the HOD to the same value of f_{sat} , reaffirming our conclusion from §3.1 that the satellite fraction is a fundamental quantity for determining the shape and amplitude of the correlation function.

Figure 5 plots the void statistics for the same HODs and luminosity samples presented in Figure 3. Panel (a) plots $P_0(r)$ for the three HOD models of the -19 sample. For $\sigma_8 = 0.9$, the $\sigma_{\log M} = 0.6$ model has smaller voids, as expected. Since f_{sat} is

the same for $\sigma_{\log M} = 0.1$ and 0.6 , the two models have equal number densities of single-galaxy halos, but the $\sigma_{\log M} = 0.6$ model allows some galaxies in lower mass halos that are more likely to be found in void interiors. However, while the sign of the effect is as expected, the magnitude is small, and only slightly larger than our statistical error bars. For example, the radius at which $P_0(r) = 10^{-3}$ changes by less than $1 h^{-1}$ Mpc. Results for the UPF (Figure 5c) and for the $M_r < -21$ sample (Figures 5b and 5d) are similar: the $\sigma_{\log M} = 0.6$ model has smaller voids, but the changes are too small to be readily detectable.

Dashed curves in each panel in Figure 5 show the $(\sigma_8, \sigma_{\log M}) = (0.7, 0.1)$ model predictions. The increased bias almost exactly compensates for the lower matter clustering amplitude. There is a slightly lower UPF for the $M_r < -19$ sample, but this difference is small, and the other predictions are nearly indistinguishable from those of the $(\sigma_8, \sigma_{\log M}) = (0.9, 0.1)$ model.

The insensitivity of void statistics to $\sigma_{\log M}$ implies that sub- M_{min} halos avoid the low density regions almost as strongly as M_{min} halos. The total number density of occupied low mass halos matters, but it makes little difference whether galaxies populate the “high end” of the low mass halo regime or populate it uniformly. Figure 6 demonstrates this point with two pedagogically illustrative model sequences. In the first, we vary f_{sat} while keeping the space density of galaxies fixed to that of the $M_r < -21$ sample. These models are no longer constrained to match the correlation function, and the role of f_{sat} is only to determine the number density of occupied halos, i.e., $n_h = (1 - f_{\text{sat}})\bar{n}_g$. For each f_{sat} , M_{min} is set by the constraint

$$n_h = \int_{M_{\text{min}}}^{\infty} \frac{dn}{dM} dM, \quad (4)$$

and all halos $M \geq M_{\text{min}}$ are given a single, central galaxy. Figure 6a plots the VPF for these models with $f_{\text{sat}} = 0$ to 0.5 in steps of 0.1 . For comparison, the VPF for the $M_r < -21$ sample with $\sigma_{\log M} = 0.1$ is shown with the open circles. The satellite fraction for this model is 0.15 , and its predictions lie in between those of the $f_{\text{sat}} = 0.1$ and $f_{\text{sat}} = 0.2$ models. The VPF monotonically increases with increasing f_{sat} because the number density of occupied halos decreases. To demonstrate the relative unimportance of spreading galaxies over a range of low mass halos, we have created a model sequence in which f_{sat} is held constant but $\langle N_{\text{cen}} \rangle_M$ is set to be a constant number less than unity at all masses. In these models, M_{min} is set by the constraint

$$n_h = \int_{M_{\text{min}}}^{\infty} \langle N_{\text{cen}} \rangle_M \frac{dn}{dM} dM, \quad (5)$$

using the nearest integer distribution to place central galaxies in halos. Figure 6b shows the VPF for models in which $f_{\text{sat}} = 0.2$ and $\langle N_{\text{cen}} \rangle_M = 1.0$ to 0.5 in steps of 0.1 . In these models the number density of occupied halos is constant, but as $\langle N_{\text{cen}} \rangle_M$ decreases the average mass of occupied halos decreases. The results in Figure 6b show a trend of lower VPF for lower $\langle N_{\text{cen}} \rangle_M$, but the amplitude of the effect is small compared to that of varying f_{sat} .

These results demonstrate that models that are constrained to match $w_p(r_p)$ offer a remarkably robust prediction of the VPF and UPF, regardless of the form of the HOD or the value of σ_8 (at least in the range $0.7 - 0.9$ considered here). We list the values of P_0 and P_U determined for the $(\sigma_8, \sigma_{\log M}) =$

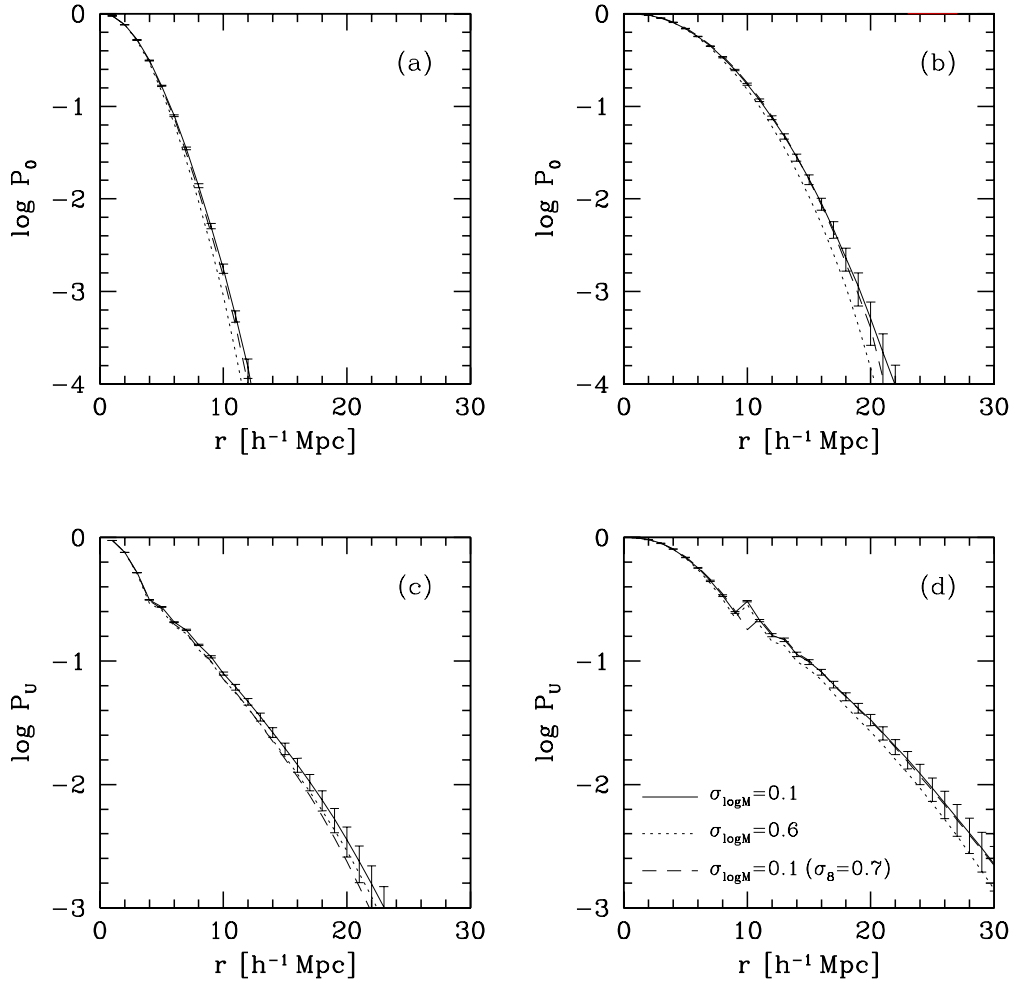


FIG. 5.— Void statistics for the HOD models shown in Figure 3. Left panels present results for $M_r < -19$, and right panels show results for $M_r < -21$. Panels (a) and (b): Void probability functions for the three HOD models shown in Figure 3. Error bars are shown for the $(\sigma_8, \sigma_{\log M}) = (0.9, 0.1)$ models only, but are the same for other models. Panels (c) and (d): Underdensity probability functions for the same models.

$(0.9, 0.1)$ models in Tables 2 and 3 for $M_r < -19$ and $M_r < -21$, respectively.

4. DENSITY DEPENDENCE OF THE HOD

Motivated by the points discussed in §1, we now consider models in which the HOD—specifically the minimum mass scale for central galaxies—changes systematically with environment. To the extent that a galaxy sample is defined by an observable property that correlates strongly with halo formation time, the dependence of formation time on large scale overdensity (Gao et al. 2005; Harker et al. 2005; Wechsler et al. 2005) will drive such variations in the HOD. The strength of this dependence increases rapidly toward lower halo masses, so it is interesting to examine environmental effects for both faint and bright galaxy samples.

Even in the deepest voids in the dark matter, halos still form (Gottlöber et al. 2003). Figure 7a shows the fraction of halos below a given overdensity as a function of halo mass. For each halo in the simulation, the surrounding dark matter density is calculated in a top-hat sphere $5 h^{-1} \text{Mpc}$ in radius. Although the choice of smoothing radius is to some degree arbitrary, we adopt $5 h^{-1} \text{Mpc}$ over a larger radius because environmen-

tal dependence in low-density regions may be sensitive not just to whether the halo resides in a void, but also to *where* in the void, and the local matter density increases closer to the edge. At $10^{11} h^{-1} M_\odot$ approximately 40% of the halos are in underdense regions, and $\sim 10\%$ are in regions with $\delta \leq -0.4$. These fractions monotonically decrease with increasing halo mass, until the fraction of halos in underdense environments is nearly zero for all halos above $10^{13} h^{-1} M_\odot$. Figure 7b plots the mass function for the halos in different environments. From left to right, the solid lines represent mass functions for halos in regions with $\delta < -0.8$ to $\delta < 0$ in steps of 0.2. Each mass function can be approximated by a power-law at low masses with an exponential cutoff at high masses (Press & Schechter 1974). The change from power-law to exponential occurs at a mass scale denoted M_* . The value of M_* for each mass function plotted in panel (b) corresponds to the mass at which the curves in panel (a) turn over and begin to approach zero. The arrows indicate M_{\min} for $M_r < -19$ (upward arrow) and $M_r < -21$ (downward arrow), indicating that bright galaxies reside in regions with matter densities $\delta \gtrsim -0.2$, but that faint galaxies reside in nearly all environments.

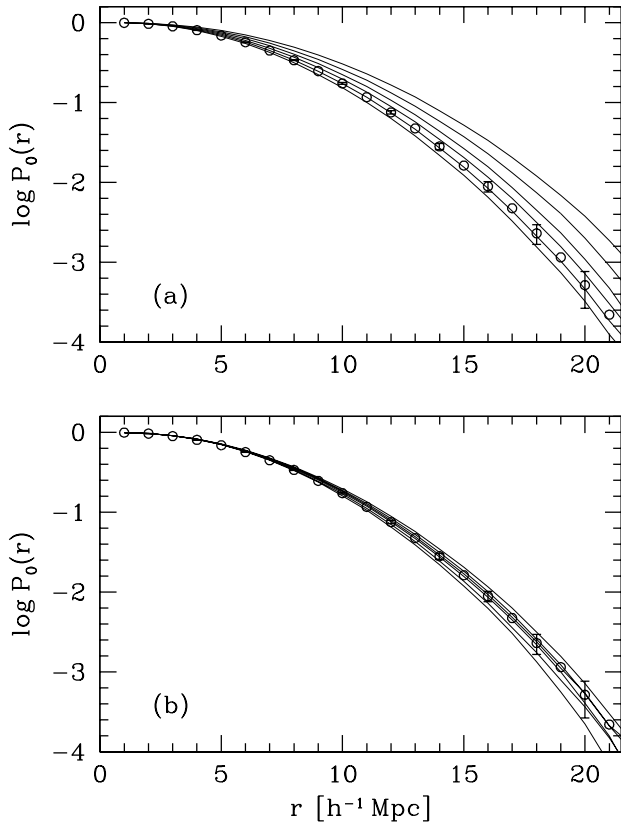


FIG. 6.— Panel (a): VPFs for models with varying f_{sat} but fixed overall space density of galaxies. From bottom to top, the 6 solid lines represent $f_{\text{sat}} = 0$ to 0.5 in steps of 0.1. The open circles represent the $M_r < -21$ results from Figure 9b, which have $f_{\text{sat}} = 0.15$. Panel (b): VPFs for models with varying $\langle N_{\text{cen}} \rangle_M$, but fixed $f_{\text{sat}} = 0.2$. From bottom to top, the solid lines represent $\langle N_{\text{cen}} \rangle_M = 0.5$ to 1.0 in steps of 0.1 (and are constant for all halo masses). The open circles are the same as panel (a).

Our model for the density dependence of halo occupation is simple: below a given density threshold δ_c , the minimum mass that can host a galaxy (in the galaxy class being modeled) increases by a factor f_{min} . For $M_r < -19$, we will examine models in which δ_c ranges from -0.8 to -0.2 and $f_{\text{min}} = 2, 4, \text{ and } \infty$ (i.e., galaxy formation is halted below δ_c for this class of galaxies). A physical model would presumably predict a smooth transition in which the probability of hosting a sample galaxy changes continuously with local density, but the quantitative effect is most likely degenerate with our two-parameter model. In our parameterization it is straightforward to isolate the two characteristics of environmental dependence: the density at which a change occurs, and magnitude of the shift in the HOD.

Although the relative number of galaxies in extremely underdense regions is low, altering the galaxy distribution in these regions does have some impact on the correlation function. Removing galaxies from anti-biased halos (and placing them in higher-density environments in order to keep the total space density of galaxies fixed) increases the overall bias of the galaxy sample. This increase can be masked to some degree by changes in other HOD parameters. For each δ_c and f_{min} we recalculate HOD parameters to obtain a minimum χ^2 fit to the SDSS $w_p(r_p)$ measurements, but we now use the populated halos of the N-body simulation to calculate $w_p(r_p)$ rather than the analytic model. We leave the value of $\sigma_{\log M}$ as a free parameter and start the minimization at the HOD for

TABLE 3
PREDICTED VOID STATISTICS FOR $M_r < -21$
GALAXIES

r [h^{-1} Mpc]	$P_0(r)$	$P_U(r)$
1	$(9.95 \pm 0.01) \times 10^{-1}$	$(9.95 \pm 0.01) \times 10^{-1}$
2	$(9.65 \pm 0.01) \times 10^{-1}$	$(9.65 \pm 0.01) \times 10^{-1}$
3	$(8.99 \pm 0.02) \times 10^{-1}$	$(8.99 \pm 0.02) \times 10^{-1}$
4	$(8.05 \pm 0.03) \times 10^{-1}$	$(8.05 \pm 0.03) \times 10^{-1}$
5	$(6.90 \pm 0.03) \times 10^{-1}$	$(6.90 \pm 0.03) \times 10^{-1}$
6	$(5.68 \pm 0.04) \times 10^{-1}$	$(5.68 \pm 0.04) \times 10^{-1}$
7	$(4.47 \pm 0.04) \times 10^{-1}$	$(4.47 \pm 0.04) \times 10^{-1}$
8	$(3.39 \pm 0.05) \times 10^{-1}$	$(3.39 \pm 0.05) \times 10^{-1}$
9	$(2.47 \pm 0.04) \times 10^{-1}$	$(2.47 \pm 0.04) \times 10^{-1}$
10	$(1.73 \pm 0.04) \times 10^{-1}$	$(3.05 \pm 0.04) \times 10^{-1}$
11	$(1.17 \pm 0.04) \times 10^{-1}$	$(2.13 \pm 0.05) \times 10^{-1}$
12	$(7.51 \pm 0.37) \times 10^{-2}$	$(1.62 \pm 0.04) \times 10^{-1}$
13	$(4.73 \pm 0.30) \times 10^{-2}$	$(1.49 \pm 0.05) \times 10^{-1}$
14	$(2.81 \pm 0.25) \times 10^{-2}$	$(1.14 \pm 0.04) \times 10^{-1}$
15	$(1.62 \pm 0.19) \times 10^{-2}$	$(9.82 \pm 0.45) \times 10^{-2}$
16	$(8.89 \pm 1.31) \times 10^{-3}$	$(8.15 \pm 0.43) \times 10^{-2}$
17	$(4.72 \pm 0.96) \times 10^{-3}$	$(6.45 \pm 0.41) \times 10^{-2}$
18	$(2.30 \pm 0.64) \times 10^{-3}$	$(5.16 \pm 0.39) \times 10^{-2}$
19	$(1.15 \pm 0.45) \times 10^{-3}$	$(4.16 \pm 0.37) \times 10^{-2}$
20	$(5.15 \pm 2.51) \times 10^{-4}$	$(3.34 \pm 0.34) \times 10^{-2}$
21	$(2.19 \pm 1.30) \times 10^{-4}$	$(2.62 \pm 0.31) \times 10^{-2}$
22	$(9.50 \pm 6.54) \times 10^{-5}$	$(2.03 \pm 0.28) \times 10^{-2}$
23	$(3.10 \pm 2.05) \times 10^{-5}$	$(1.59 \pm 0.25) \times 10^{-2}$
24	$(1.20 \pm 1.20) \times 10^{-5}$	$(1.23 \pm 0.23) \times 10^{-2}$
25	$(3.00 \pm 3.00) \times 10^{-6}$	$(9.31 \pm 2.01) \times 10^{-3}$

the density-independent HOD found in the previous section for $\sigma_{\log M} = 0.1$.

4.1. Results for $M_r < -19$

Figure 8 shows several examples of $w_p(r_p)$ for density-dependent models of the $M_r < -19$ sample. Panel (a) plots the correlation functions for $f_{\text{min}} = \infty$ and $\delta_c = -0.8, -0.6, \text{ and } -0.4$. The SDSS data are also shown for comparison. For $\delta_c = -0.8$, the change in the correlation function is negligible. For $\delta_c = -0.6$, the exclusion of low-density halos noticeably increases the large-scale amplitude of $w_p(r_p)$. This effect is magnified for the $\delta_c = -0.4$ model, and the resulting correlation function is clearly excluded by the data. The $\Delta\chi^2$ between $\delta_c = -0.8$ and -0.6 is 1.4, while for $\delta_c = -0.4$ the $\Delta\chi^2 \approx 10$. Panel (b) in figure 8 shows the results for $f_{\text{min}} = 2$. This more moderate model of density dependence, where galaxy formation is suppressed but not eliminated in low density environments, has a smaller effect on $w_p(r_p)$ at the same value of δ_c .

The effect of density dependence on $w_p(r_p)$ can be interpreted through the “voided Poisson” model of Babul (1991) and Babul & White (1991). Removing galaxies from low-density regions makes the voids larger. Since the galaxy number density is held fixed, a simple random distribution of the displaced galaxies throughout the volume not occupied by the voids increases the clustering at scales less than the characteristic size of the voids. The stronger the density dependence, the higher the boost in $w_p(r_p)$. Appendix A shows that this simple model provides a surprisingly accurate description of our numerical results.

Figure 9 shows the VPFs for $\sigma_8 = 0.9$ models with the three values of f_{min} . In each panel, the filled circles with error bars show the results for $\sigma_{\log M} = 0.1$ from Figure 5. The lines,

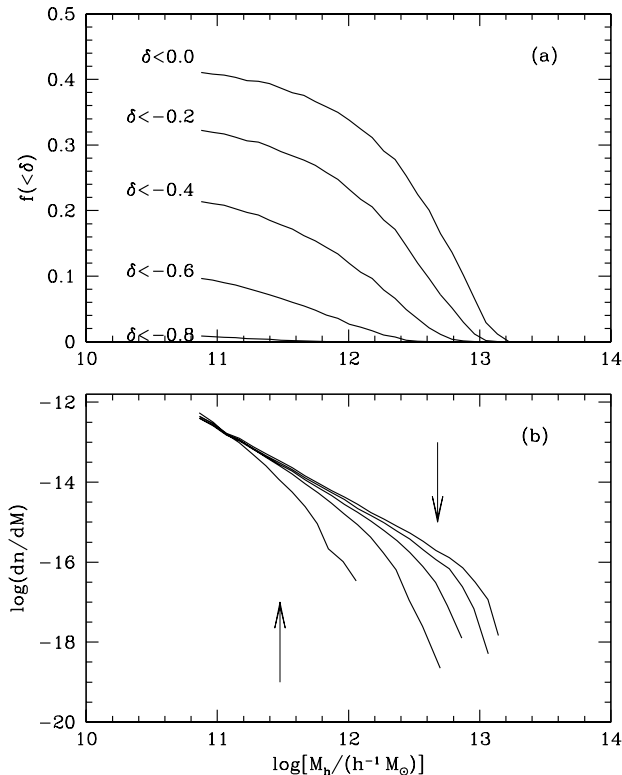


FIG. 7.— Panel (a): Fraction of halos that lie in regions below a given matter density as a function of halo mass. The top line represents the fraction of halos that lie in underdense ($\delta < 0$) regions as a function of halo mass. Subsequent lines present results for lower density contrasts as labeled in the panel. Panel (b): Mass functions of halos in low-density environments. Solid lines show the mass functions for halos in $\delta < -0.8$ regions (far left) to $\delta < 0$ (far right), corresponding to the bottom and top lines in panel (a) respectively. The upward pointing arrow marks the location of M_{\min} for the $M_r < -19$ sample, and the downward arrow indicates M_{\min} for $M_r < -21$ galaxies (for $\sigma_{\log M} = 0.1$). For all density calculations, the smoothing radius is $5 h^{-1}$ Mpc.

from bottom to top, plot $P_0(r)$ for $\delta_c = -0.8, -0.6, -0.4$, and -0.2 . (from lowest to highest). Panel (a) shows the results for $f_{\min} = 2$. For $\delta_c = -0.8$ (the lowest line), the effect on P_0 is negligible. This is to be expected from Figure 7 because nearly all halos above M_{\min} are in regions above $\delta = -0.8$ anyway. For $\delta_c \geq -0.6$, the change in P_0 is substantial; at $P_0 = 10^{-4}$, the change in radius is nearly $2 h^{-1}$ Mpc, while at $12 h^{-1}$ Mpc, the change in P_0 is ~ 1 dex. The VPFs exhibit little further change above $\delta_c = -0.6$ because halos above $2M_{\min}$ are still common at these densities. The effect of environmental dependence on P_0 thus “saturates” at a density that we denote δ_s . In the context of Figure 7, if $M_{\min} < M_*(\delta_c) < f_{\min}M_{\min}$, then the density dependence eliminates most halos that would have been able to host galaxies because $f_{\min}M_{\min}$ is on the exponential cutoff of the mass function for regions with $\delta < \delta_c$. This significantly increases the probability that a low-density region that was otherwise occupied is now counted as a void. If both M_{\min} and $f_{\min}M_{\min}$ are below M_* , then the density dependence moves the minimum mass scale along the power-law portion of the halo mass function, but not into the exponential cutoff. The number of halos massive available to host galaxies is reduced, but the fractional change in galaxy-hosting halos is much smaller. Thus the likelihood of increasing the sizes of voids is low. In order to further expand the voids, f_{\min} must be increased.

Figure 5b plots the results for $f_{\min} = 4$. For $\delta_c = -0.8$, the

VPF is similar to that of $f_{\min} = 2$, and the VPF again changes dramatically for $\delta_c = -0.6$. Because of the higher f_{\min} , “saturation” sets in at a higher threshold density $\delta_c \approx -0.4$. At this δ_c , the VPF is greatly amplified relative to the density-independent models; the change in the radius at which $P_0 = 10^{-4}$ is $\sim 3.5 h^{-1}$ Mpc, and the increase in P_0 at $12 h^{-1}$ Mpc is nearly 1.5 dex. Increasing f_{\min} further effectively removes the saturation effect. Panel (c) shows the results for $f_{\min} = \infty$. This model evacuates regions below δ_c completely, regardless of halo mass. At a fixed radius the probability of finding a void increases monotonically with δ_c .

Figure 10 presents the UPF results for the same models. The lines and points in each panel correspond to the same models at Figure 9. Density dependence in the HOD has a different effect on the UPF than on the VPF. An increase in δ_c at a given f_{\min} always reduces the number of galaxies in a region of low density, even though that region may not be a completely empty void. Therefore the saturation effect seen in the VPF is not as striking for the UPF. In panel (a), increasing δ_c always results in a higher UPF, but the difference between the models gets smaller at higher δ_c . As with the VPF, the increase in P_U is larger for higher f_{\min} . At $(f_{\min}, \delta_c) = (4, -0.4)$, the change in r with respect to the density-independent models is $5 h^{-1}$ Mpc for $P_U = 10^{-2}$. At $r = 20 h^{-1}$ Mpc, the increase in P_U is 0.7 dex.

4.2. Results for $M_r < -21$

Our density-dependent HOD models for the brighter, $M_r < -21$ galaxies employ the same values of f_{\min} , but larger values of δ_c are required to produce a noticeable change in the galaxy distribution. For conciseness, we present results for $f_{\min} = 2$ only, but increasing f_{\min} has the same qualitative effect as shown for the $M_r < -19$ sample. Figure 11a plots $w_p(r_p)$ for $\delta_c = -0.2, 0$, and $+0.2$. Recall that the density-independent HOD fits from Figure 3 were statistically acceptable, but that the large-scale amplitude of the models was slightly below the observed level. Boosting $w_p(r_p)$ by adding density-dependence to the HOD decreases χ^2 for $\delta_c \sim 0$, but the fit becomes poor for $\delta_c \gtrsim +0.3$. Figure 11b plots $P_0(r)$ for models with $\delta_c = -0.4$ to $+0.4$ in steps of 0.2. At $\delta_c = -0.4$ there is no change in the sizes of voids. The effect of environmental dependence does not become significant until $\delta_c \geq -0.2$. As with the $M_r < -19$ models, the effect on the VPF reaches a saturation limit at high δ_c . For $f_{\min} = 2$ the saturation density is $\delta_s = 0$. Figure 11c plots $P_U(r)$ for the same values of δ_c . As with the faint galaxy sample, as $P_U(r)$ increases monotonically as δ_c increases. The effect on the UPF also becomes detectable at $\delta_c \geq -0.2$.

Figure 12 roughly delineates the areas in parameter space that produce weak and strong effects on galaxy clustering. The gray lines show the limit where density dependence produces measurable changes in the void statistics. The lower gray line is for $M_r < -19$ and the upper gray line is for $M_r < -21$. Above the gray lines, there is a region of parameter space in which the effect on $w_p(r_p)$ is weak, defined as $\Delta\chi^2 < 4$ with respect to the best-fit density-independent model. The black lines denote the transition between strong and weak influence on $w_p(r_p)$. For low f_{\min} , the region of weak dependence spans a larger range in δ_c . As f_{\min} increases, the lines flatten out at $\delta_c = -0.5$ and $+0.1$ for the -19 and -21 samples respectively. Below these densities there are relatively few halos above M_{\min} ; there are enough to alter the distribution of voids but not to change the overall bias of the

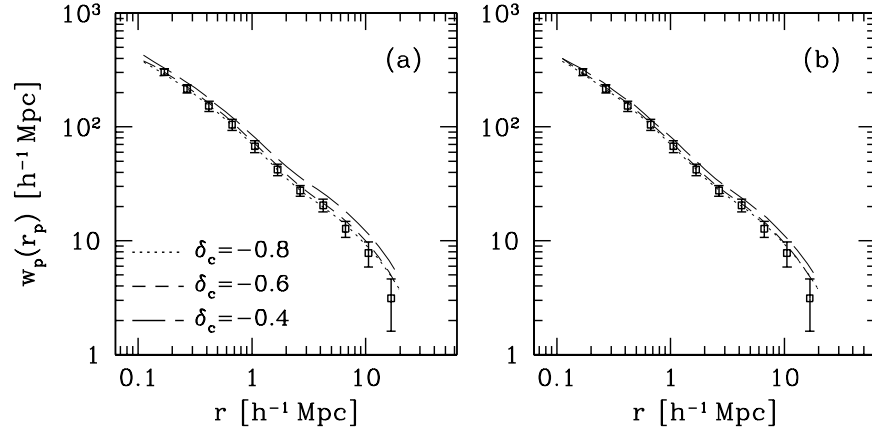


FIG. 8.— Projected correlation functions for density-dependent HOD models of the $M_r < -19$ sample. (a) Models in which $M_r < -19$ galaxies are completely suppressed ($f_{\min} = \infty$) below critical densities $\delta_c = -0.8, -0.6,$ and -0.4 . Points with error bars are the SDSS data. (b) Models in which the minimum host halo mass increases by a factor $f_{\min} = 2$ below the same values of δ_c .

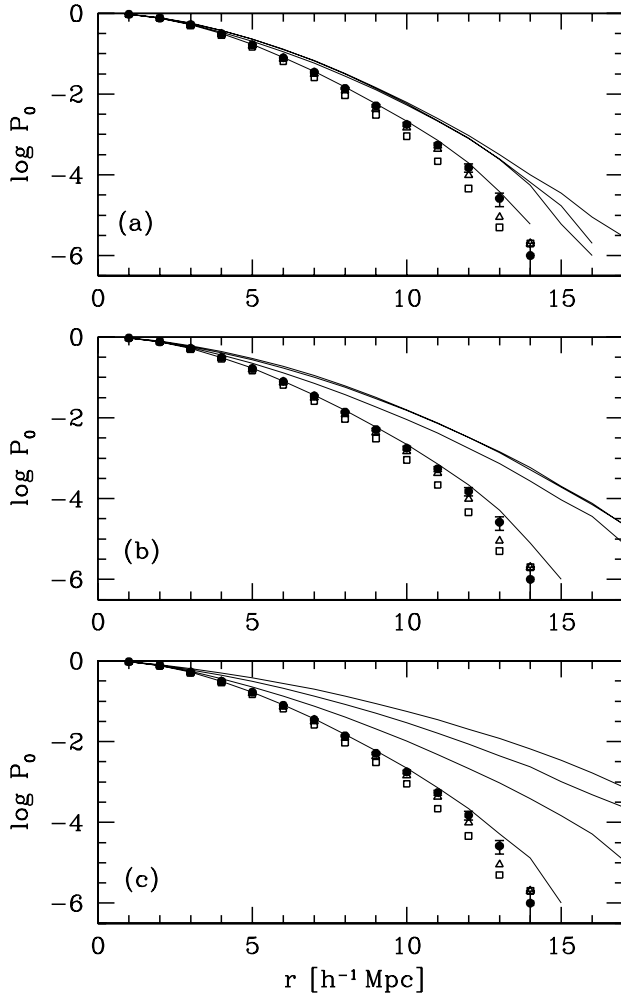


FIG. 9.— Void probability functions for density-dependent HOD models of the $M_r < -19$ sample. In all three panels, lines are density-dependent HOD models while points show the three models, from Figure 5a. Solid points with error bars represent the $(\sigma_8, \sigma_{\log M}) = (0.9, 0.1)$ model, open triangles are the $(0.9, 0.6)$ model, and open squares are the $(0.7, 0.1)$ model. Panel (a): Models with $f_{\min} = 2$. The four lines, from bottom to top, show results for $\delta_c = -0.8, -0.6, -0.4,$ and -0.2 . Panel (b): Models with $f_{\min} = 4$ for the same values of δ_c . Panel (c): Models with $f_{\min} = \infty$ for the same values of δ_c .

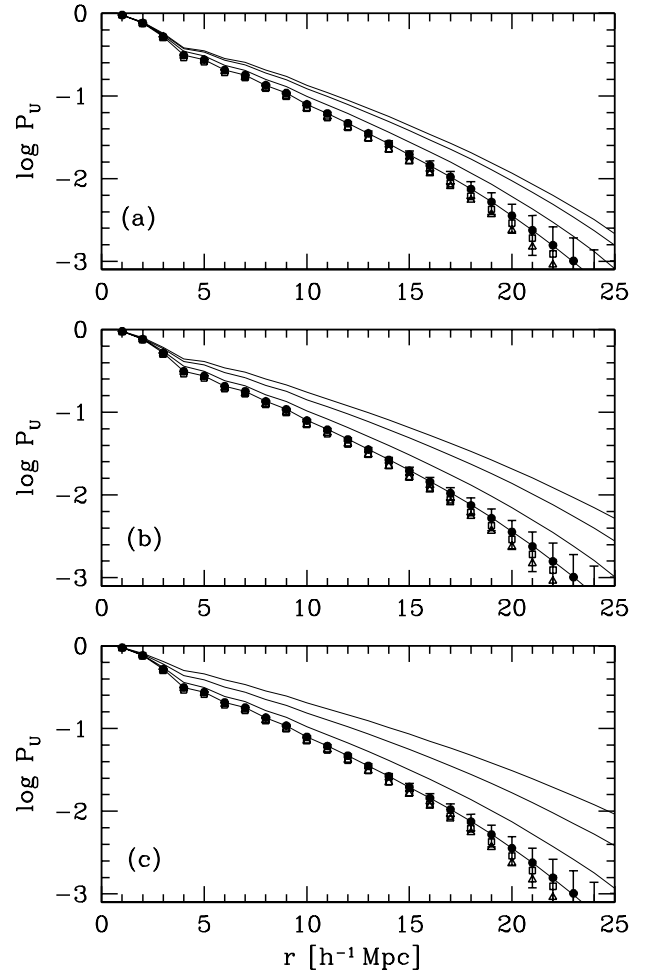


FIG. 10.— Undersdensity probability functions for density-dependent HOD models of the $M_r < -19$ sample. In all three panels, lines are density-dependent HOD models while points show the three models from Figure 5a. Solid points with error bars represent the $(\sigma_8, \sigma_{\log M}) = (0.9, 0.1)$ model, open triangles are the $(0.9, 0.6)$ model, and open squares are the $(0.7, 0.1)$ model. Panel (a): Models with $f_{\min} = 2$. The four lines, from bottom to top, show results for $\delta_c = -0.8, -0.6, -0.4,$ and -0.2 . Panel (b): Models with $f_{\min} = 4$ for the same values of δ_c . Panel (c): Models with $f_{\min} = \infty$ for the same values of δ_c .

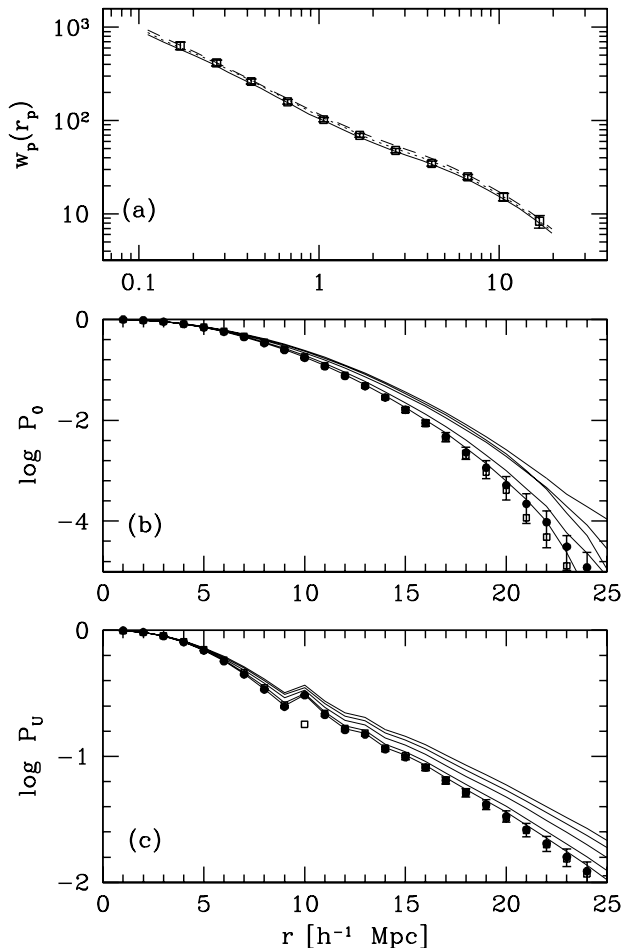


FIG. 11.— Clustering statistics for density-dependent HOD models of the $M_r < -21$ sample. All models have $f_{\min} = 2$. Panel (a): Projected correlation function. Points with errors are the SDSS data from Figure 3. Line types are results for $\delta_c = -0.2$ (solid), $\delta_c = 0$ (dotted), and $\delta_c = +0.2$ (dashed). Panel (b): Void probability functions. Solid points with error are results from Figure 5b for $(\sigma_8, \sigma_{\log M}) = (0.9, 0.1)$. Open squares plot the results for $(0.7, 0.1)$. The five lines show results for $\delta_c = -0.4$ to $+0.4$ in steps of 0.2. Panel (c): Under-density probability functions for the same models shown in panel (b). The open squares are plotted but cannot be distinguished from the other points. As with the -19 samples, increasing δ_c corresponds to increasing VPF and UPF.

galaxy sample.

5. SUMMARY AND DISCUSSION

We have examined how non-linear galaxy bias, described in the HOD framework, affects the distribution of void sizes once the galaxy number density \bar{n}_g and projected correlation function $w_p(r_p)$ are imposed as observational constraints. After choosing HOD parameters that reproduce these observables as measured for SDSS galaxy samples with $M_r < -19$ and $M_r < -21$, we compute VPFs and UPFs by populating the halos of a large, high-resolution N-body simulation of a Λ CDM cosmological model. We consider “standard” models in which the galaxy HOD is independent of environment and models that incorporate a simple form of environmental variation.

Our parameterization of the HOD incorporates a smoothly truncated step function for the mean occupation $\langle N_{\text{cen}} \rangle_M$ of central galaxies and a smoothly truncated power-law for the mean occupation of $\langle N_{\text{sat}} \rangle_M$ of satellites. Void statistics are sensitive to $\langle N_{\text{cen}} \rangle_M$, since halos massive enough to host mul-

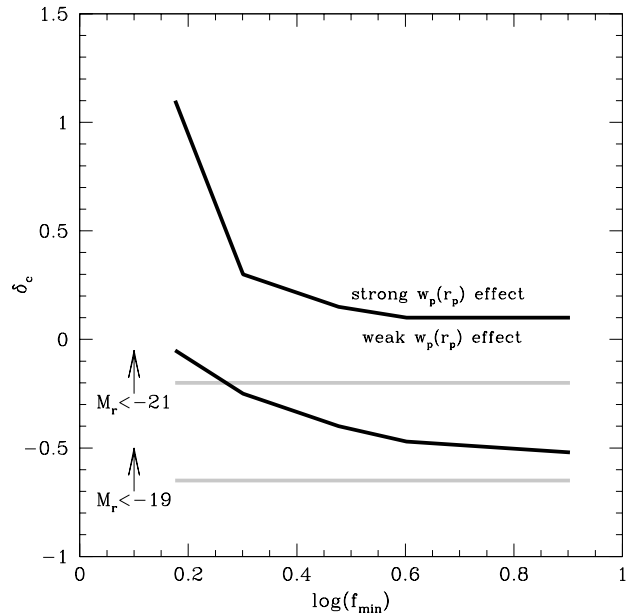


FIG. 12.— Regions in the $f_{\min} - \delta_c$ parameter space where environmental dependence of the HOD has a readily measurable impact on void statistics or on the projected correlation function, for galaxies with $M_r < -19$ (lower lines) or $M_r < -21$ (upper lines). The gray lines denote the space above which the effect on the void statistics is measurable. The black lines denote the space above which the effect on $w_p(r_p)$ is strong ($\Delta\chi^2 > 4$). Between the gray and black lines are the regions of parameter space in which environmental dependence is detectable with void statistics but does not significantly affect the correlation function.

iple galaxies generally reside in overdense regions. If the width of the cutoff in $\langle N_{\text{cen}} \rangle_M$ is specified, then the cutoff mass scale M_{\min} is tightly constrained by the combination of $w_p(r_p)$ and \bar{n}_g , and variation of M_{\min} in the allowed range produces almost no change in the VPF or UPF. Broadening the cutoff in $\langle N_{\text{cen}} \rangle_M$ allows some galaxies to occupy lower mass, less biased halos, slightly reducing void sizes, but the effects are smaller than the statistical errors expected from the SDSS.

More generally, fitting the projected correlation function tightly constrains the fraction f_{sat} of galaxies that are satellites, with $f_{\text{sat}} \approx 0.23$ and $f_{\text{sat}} \approx 0.15$ for $M_r < -19$ and $M_r < -21$, respectively, assuming $\sigma_8 = 0.9$. Once f_{sat} is pinned down by $w_p(r_p)$, the \bar{n}_g constraint determines the space density of single-occupancy halos, and because these are already in the mass regime where spatial bias depends weakly on halo mass, the void statistics are essentially fixed. When σ_8 is lowered to 0.7, the HOD changes required to increase bias of the correlation function almost exactly compensate the reduced void sizes in the matter distribution, leading to nearly identical galaxy void statistics. Thus, the assumption of an environment-independent HOD that reproduces the observed $w_p(r_p)$ and \bar{n}_g leads to a robust prediction of the VPF and UPF.

Void statistics are, however, sensitive to differences in the minimum halo mass between low and high density regions. We have introduced parameterized models that incorporate such environment-dependent HODs by changing the cutoff mass M_{\min} by a factor f_{\min} in regions where the large scale density contrast δ (defined with a $5h^{-1}$ Mpc tophat) is below a critical value δ_c . For large values of δ_c (above ~ -0.5 for $M_r < -19$ and ~ 0.1 for $M_r < -21$, depending on f_{\min}), density dependence of the HOD changes the correlation function in a way that cannot be masked by varying other HOD parameters. However, there is a substantial range of (f_{\min}, δ_c)

values for which density dependence of the HOD has a negligible impact on $w_p(r_p)$ but a readily measurable impact on the VPF and UPF. Furthermore, the two void statistics provide somewhat complementary information, allowing one to estimate separately the critical density and the magnitude of the shift in M_{\min} .

Because they are sensitive to environmental variations of the HOD, void statistics can remove one source of uncertainty in deriving cosmological constraints from observed galaxy clustering. For a specific example, recall that the $\sigma_8 = 0.7$ model underpredicts $w_p(r_p)$ for $M_r < -19$ galaxies if we assume that the HOD is independent of environment (Fig. 3a). Raising M_{\min} in low density regions could boost the galaxy bias factor and thereby improve the agreement between this model and the SDSS $w_p(r_p)$ measurements. However, any change large enough to alter the correlation function at this level should be easily detected or ruled out by void statistics. There may be environmental variations in high mass halos that could affect $w_p(r_p)$ without altering void statistics, but voids are the “canary in the coal mine” for any changes in the large scale galaxy bias factor driven by suppression (or enhancement) of galaxy formation in low density regions.

In hierarchical scaling models, the void probability function can be written as an infinite sum of all n -point correlation functions, which can in turn be expressed as products of the two-point correlation function (White 1979; Fry 1986). Conroy et al. (2005) argue that the VPF provides little new information about the HOD once $w_p(r_p)$ has been accurately measured because of this hierarchical scaling. While we agree that the VPF is essentially determined by matching $w_p(r_p)$ for environment-independent HOD models, we do not think that hierarchical scaling alone explains this result. First, one could create two HOD models with virtually identical void statistics but very different correlation functions simply by moving satellite galaxies to more massive halos while keeping central galaxy occupations fixed. Conversely, our (f_{\min}, δ_c) models include cases with very similar correlation functions but substantially different VPFs. Hierarchical scaling arguments correctly predict the sign of the VPF changes in Figures 9 and 11 — models with higher $w_p(r_p)$ have larger voids — but they do not explain the magnitude of these changes. The relation between void probabilities and the two-point correlation function depends not on the hierarchical *ansatz* alone but on the specific amplitudes that relate n -point functions to the

two-point function, and these can themselves change with the HOD.

Recent N-body studies show a strong correlation between halo formation time and large scale environment for low mass halos (Gao et al. 2005; Harker et al. 2005; Wechsler et al. 2005; Zhu et al. 2006) — in particular, the oldest halos avoid low density environments. At fixed halo mass, an older halo could plausibly host a more luminous central galaxy because of more efficient gas cooling and cannibalism of satellites, or it could host a less luminous central galaxy because of greater fading of stellar populations (see Zhu et al. 2006 for example calculations). Precise measurements of void statistics for the SDSS galaxy samples modeled here will provide an excellent probe of the link between halo formation time and r -band galaxy luminosity. A strong correlation between the two would cause significant departures from the “standard” (environment-independent) HOD predictions presented in Tables 2 and 3, while good agreement with these predictions would indicate that luminosity is determined by halo mass with little dependence on formation epoch. Extending these arguments and analyses to samples of lower luminosity and additional selection criteria such as color or surface brightness will allow detailed exploration of the links between a galaxy’s present day properties and the assembly history of its dark matter halo.

JT would like to thank Charlie Conroy for many useful discussions. JT and DW acknowledge support from NSF grant AST-0407125. JT was supported by a Distinguished University Fellowship at Ohio State University during the course of this work. Portions of this work were performed under the auspices of the U.S. Dept. of Energy, and supported by its contract #W-7405-ENG-36 to Los Alamos National Laboratory. Computational resources were provided by the LANL open supercomputing initiative.

APPENDIX

THE VOIDED POISSON MODEL

For a random distribution of points the correlation function is zero at all r . If spherical regions of radius R_V are voided, and the displaced galaxies randomly distributed through the non-void regions, a correlation is induced in the points which is non-zero at scales smaller than $2R_V$. Babul (1991) presents the resulting correlation function for a given void radius R_V as

$$1 + \xi_V(r, R_V) = \exp \left\{ \frac{f_V}{2} \left[\left(\frac{r}{2R_V} \right)^3 - 3 \left(\frac{r}{2R_V} \right) + 2 \right] \right\} \quad (\text{A1})$$

for $r \leq 2R_V$, and $1 + \xi(r, R_V) = 1$ otherwise. The parameter f_V is the filling factor of the voids, defined as $f_V = 4\pi R_V^3 n_V / 3$, where n_V is the number density of non-overlapping voids.

Originally proposed as a model for the clustering of Lyman- α absorption clouds with “spheres of avoidance” carved out by quasars, this model is also applicable to galaxy clustering in our density-dependent HOD models. Lowering the efficiency of galaxy formation in low-density regions expands cosmic voids, as demonstrated in Figures 9 and 11. The number density of voids can be derived from the VPF by

$$\begin{aligned} n_V(R_V) &= P_0(R_V) V_g^{-1} \\ &\approx P_0(R_V) \frac{3\pi^2 (n'V)^3}{32 V} \end{aligned} \quad (\text{A2})$$

where V denotes spherical volume, V_g is the volume within which a void with radius R_V can be moved without coming into contact with a galaxy, and

$$n'(R_V) = \frac{d \ln P_0(R_V)}{4\pi R_V^2 dR_V} \quad (\text{A3})$$

(Betancort-Rijo 1990; Patiri et al. 2004). The clustering of the voided Poisson model assumes that the void regions are created from initially filled regions, while the voids in the density-dependent HOD models are simply enlarged. For the filling factor required in equation (A1), we take the difference between n_V inferred from the density-dependent model and the density-independent model. This gives us the excess number density of voids created by the density-dependence. To calculate the clustering induced by spectrum of voids of varying sizes, we integrate equation (A1) over R_V ;

$$1 + \xi_V(r) = \frac{\int [1 + \xi_V(r, R_V)] \frac{dn_V}{dR_V} dR_V}{\int \frac{dn_V}{dR_V} dR_V}. \quad (\text{A4})$$

The clustering boost induced by the voids applies only to the two-halo term of the correlation; the density of occupied halos in the inter-void space is increased, but the pairs within a single halo are not altered. The new two-halo term is

$$1 + \xi_{2h}^{(V)}(r) = [1 + \xi_V(r)][1 + \xi_{2h}(r)], \quad (\text{A5})$$

where $\xi_{2h}(r)$ is the density-independent two-halo term, which is calculated analytically.

Figure A13 shows the results of the model for density-dependent models of the $M_r < -21$ sample with $f_{\min} = 4$. To calculate n_V , we use the VPFs obtained from the N-body results in equations (A2) and (A3). Panel (a) plots $\xi(r)$ for models with $\delta_c = 0$. The filled circles show the results for the density-independent model. This value of δ_c produces a weak boost in the large-scale clustering, shown by the solid line. The dotted line, showing the results of the voided Poisson model, is difficult to see underneath the N-body results. Panel (b) plots the same results but for more extreme models with $\delta_c = 0.4$. The effect on $\xi(r)$ is more pronounced, but it is still well described by the voided Poisson model. Panels (c) and (d) show $\Delta[\log \xi(r)]$ with respect to the density-independent model for the density-dependent N-body results and the model calculations. Panel (d) plots the results for $\delta_c = 0$, which boosts the large-scale amplitude of $\xi(r)$ by ~ 0.06 dex. The boost abruptly goes away at $r < 1.5 h^{-1}$ Mpc, demonstrating that the change in clustering applies to the two-halo term only. For $\delta_c = 0.4$, shown in panel (d), the boost is ~ 0.15 dex for the large-scale $\xi(r)$. The model agrees well with the N-body results, but turns over at $r > 20 h^{-1}$ Mpc. This discrepancy is likely a result of truncating the integral in equation (A4) at $25 h^{-1}$ Mpc, which is the limit of our N-body calculations of the VPF.

The voided Poisson model offers an accurate quantitative explanation of the effect of our density-dependent HOD models on the correlation function. Unfortunately, as presented in this Appendix it cannot be used for full analytic modeling of the effect of density dependence without the use of N-body simulations, which were used here to obtain n_V . The need for N-body simulations could be circumvented with analytic approximations of the conditional mass function (Sheth & Tormen 2002; Gottlöber et al. 2003; Patiri et al. 2004), but it is unclear whether these approximations have the necessary accuracy for use as a tool for constraining density dependence with $w_p(r_p)$ measurements. Further investigation may prove fruitful.

REFERENCES

- Babul, A. 1991, MNRAS, 253, 31
 Babul, A. & White, S. D. M. 1991, MNRAS, 248, 177
 Benson, A. J., Cole, S., Frenk, C. S., Baugh, C. M., & Lacey, C. G. 2000, MNRAS, 311, 793
 Benson, A. J. 2001, MNRAS, 325, 1039
 Benson, A. J., Frenk, C. S., Baugh, C. M., Cole, S., & Lacey, C. G. 2003, MNRAS, 343, 679
 Berlind, A. A., & Weinberg, D. H. 2002, ApJ, 575, 587
 Berlind, A. A., Weinberg, D. H., Benson, A. J., Baugh, C. M., Cole, S., Davé, R., Frenk, C. S., Katz, N., & Lacey, C. G. 2003, ApJ, 593, 1
 Berlind, A. A., Blanton, M. R., Hogg, D. W., Weinberg, D. H., Davé, R., Eisenstein, D. R., & Katz, N. 2005, ApJ, 629, 625
 Betancort-Rijo, J. 1990, MNRAS, 246, 608
 Blanton, M. R., Eisenstein, D. J., Hogg, D. W., & Zehavi, I. 2004, ApJ, submitted, (astro-ph/0411037)
 Blanton, M. R., Eisenstein, D. J., Hogg, D. W., Schlegel, D. J., & Brinkmann, J. 2003, ApJ, 629, 143
 Bond, J. R., Cole, S., Efstathiou, G., & Kaiser, N. 1991, ApJ, 379, 440
 Bullock, J. S., Kolatt, T. S., Sigad, Y., Somerville, R. S., Klypin, A. A., Primack, J. R., Dekel, A. 2001, MNRAS, 321, 559
 Bullock, J. S., Kravtsov, A. V., & Weinberg, D. H. 2001, ApJ, 548, 33
 Colless, M. et. al. 2001, MNRAS, 328, 1039
 Conroy, C., Coil, A. L., White, M., Newman, J. A., Yan, R., Cooper, M. C., Gerke, B. F., Davis, M., & Koo, D. C. 2005, ApJ, 635, 990
 Davis, M., Efstathiou, G., Frenk, C. S., & White, S. D. M. 1985, ApJ, 292, 371
 de Lapparent, V., Geller, M. J., & Huchra, J. P. 1991, ApJ, 369, 273
 Einasto, J., Einasto, M., Graman, M., & Saar, E. 1991, MNRAS, 248, 593
 El-Ad, H. & Piran, T. 1997, ApJ, 491, 421
 Fry, J. N. 1986, ApJ, 306, 358
 Gao, L., Springel, V., & White, S. D. M. 2005, MNRAS, 363, 66
 Gottlöber, S., Lokas, E. L., Klypin, A., & Hoffman, Y. 2003, MNRAS, 344, 715
 Guzik, J. & Seljak, U. 2002, MNRAS, 335, 311
 Harker, G., Cole, S., Helly, J., Frenk, C. S., & Jenkins, A., 2005, MNRAS, submitted (astro-ph/0510488)
 Hoefl, M., Yepes, G., Gottlöber, S., & Springel, V. 2005, MNRAS, submitted, (astro-ph/0501304)
 Hoyle, F. & Vogeley, M. S. 2004, ApJ, 607, 751
 Hoyle, F. & Vogeley, M. S. 2002, ApJ, 566, 641
 Hoyle, F., Rojas, R. R., Vogeley, M. S., & Brinkmann, J. 2005, ApJ, 620, 618
 Jenkins, A., Frenk, C. S., White, S. D. M., Colberg, J. M., Cole, S., Evrard, A. E., Couchman, H. M. P., & Yoshida, N. 2001, MNRAS, 321, 372
 Kaiser, N. 1984, ApJ, 294, L9
 Kauffmann, G. & Fairall, A. P. 1991, MNRAS, 248, 313
 Kauffmann, G. & Melott, A. L. 1991, ApJ, 343, 415
 Kauffmann, G., Nusser, A., & Steinmetz, M. 1997, MNRAS, 286, 795
 Kirshner, R. P., Oemler, A., Schechter, P., & Schectman, S. A. 1987, ApJ, 314, 493
 Kravtsov, A. V., Berlind, A. A., Wechsler, R. H., Klypin, A. A., Gottlöber, S., Allgood, B., Primack, J. R. 2004, ApJ, 609, 35
 Lemson, G. & Kauffmann, G. 1999, MNRAS, 302, 111
 Lin, Y.-T., Mohr, J. J., & Stanford, S. S. 2004, ApJ, 610, 745
 Little, B. & Weinberg, D. H. 1994, MNRAS, 267, 605
 Ma, C. & Fry, J. N. 2000, ApJ, 543, 503
 Navarro, J. F., Frenk, C. S., & White, S. D. M. 1997, ApJ, 490, 493

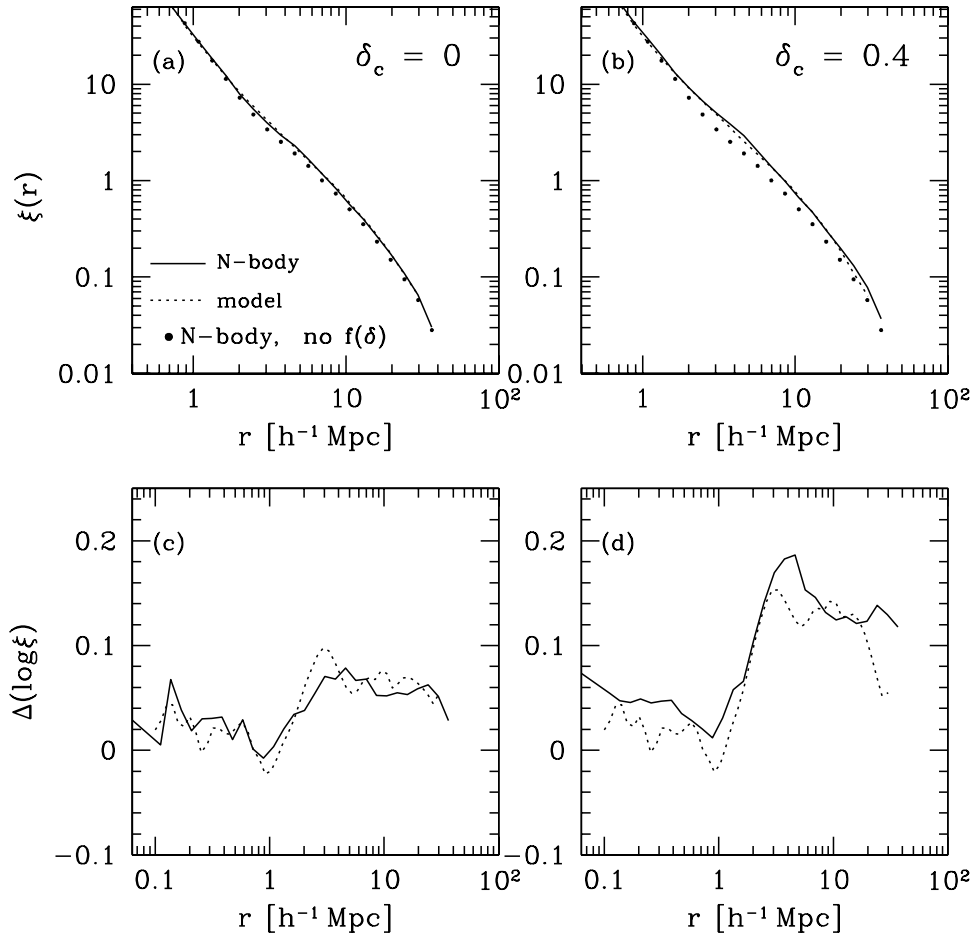


FIG. A13.— Results of the voided Poisson model of Appendix A. All panels show results for models of the $M_r < -21$ sample with $f_{\min} = 4$. Panel (a): The solid line plots N-body results for $\xi(r)$ with $\delta_c = 0$, i.e., M_{\min} increases in all regions below the mean density on the $5 h^{-1}$ Mpc scale. The dotted line shows the analytic calculation. Circles plot the N-body results for the model with no density dependence. Panel (b): Same as (a), but with $\delta_c = 0.4$. Panel (c): The solid line plots the difference in $\log \xi$ between density-dependent N-body results and density-independent N-body results from panel (a). The dotted line plots the difference between the analytic calculation and the density-independent results. Panel (d): Same as (c), but for $\delta_c = 0.4$.

- Norberg, P. et al. 2001, MNRAS, 328, 64
 Patiri, S. G., Betancort-Rijo, J. E., & Prada, F. 2004, ApJ, submitted, (astro-ph/0407513)
 Peacock, J. A., Smith, R. E. 2000, MNRAS, 318, 1144
 Percival, W. J. et al. 2002, MNRAS, 337, 1068
 Press, W. H. & Schechter, P. 1974, ApJ, 187, 425
 Rood, H. J. 1988, ARA&A, 26, 245
 Ryden, B. S. & Turner, E. L. 1984, ApJ, 287, 159
 Sanchez, A. G., Baugh, C. M., Percival, W. J., Peacock, J. A., Padilla, N. D., Cole, S., Frenk, C. S., & Norberg, P. 2005, MNRAS, 366, 189
 Scoccimarro, R., Sheth, R. K., Hui, L., & Jain, B. 2001, ApJ, 546, 20
 Seljak U. & Zaldarriaga M. 1996, ApJ, 469, 437
 Seljak, U. 2000, MNRAS, 318, 203
 Seljak, U., & Warren, M. S. 2004, MNRAS, 355, 129
 Sheth, R. K. & Tormen, G. 2002, MNRAS, 329, 61
 Sheth, R. K. & Tormen, G. 2004, MNRAS, 350, 1385
 Somerville, R. S. 2000, ApJ, 572, 23
 Spergel, D. N., et al. 2003, ApJ, 148, 175
 Springel, V. et al. 2005, Nature, 435, 629
 Tegmark, M., et al. 2004a, ApJ, 606, 702
 Tinker, J. L., Weinberg, D. H., Zheng, Z., & Zehavi, I. 2005, ApJ, 631, 41
 Tinker, J. L., Weinberg, D. H., & Zheng, Z. 2005, MNRAS, accepted, (astro-ph/0501029)
 van den Bosch, F. C., Yang, X., & Mo, H. J. 2003, MNRAS, 345, 723
 Vogeley, M. S., Park, C., Geller, M. J., & Huchra, J. P. 1992, ApJ, 391, L5
 Vogeley, M. S., Geller, M. J., Park, C., & Huchra, J. P. 1994, AJ, 108, 745
 Warren, M. S. & Salmon, J. K. 1993, in Supercomputing '93. IEEE Comp.Soc., Los Alamos
 Warren, M. S., Abazajian, K., Holz, D. E., & Teodoro, L. 2005, ApJL, submitted, (astro-ph/0506395)
 Weinberg, D. H. & Cole, S. 1992, MNRAS, 259, 652
 Weinberg, D. H., Davé, R., Katz, N., & Hernquist, L. 2004, ApJ, 601, 1
 White, S. D. M. 1979, MNRAS, 186, 145
 White, S. D. M. 1996, in Cosmology and Large Scale Structure, eds. R. Schaefer, J. Silk, M. Spiro, & J. Zinn-Justin, Elsevier, Amsterdam, p. 349, (astro-ph/9410043)
 Wechsler, R. H., Zentner, A. R., Bullock, J. S., & Kravtsov, A. V., 2005, ApJ, submitted (astro-ph/0512416)
 Yang, X. H., Mo, H. J., & van den Bosch, F. C. 2003, MNRAS, 339, 1057
 Yang, X., Mo, H. J., Jing, Y. P., van den Bosch, F. C., & Chu, X. Q. 2004, MNRAS, 350, 1153
 York, D. et al. 2000, AJ, 120, 1579
 Zehavi, I., Weinberg, D. H., Zheng, Z., Berlind, A. A., Frieman, J. A., et al. 2004, ApJ, 608, 16
 Zehavi, I., Zheng, Z., Weinberg, D. H., Frieman, J. A., Berlind, A. A., et al. 2005, ApJ, 630, 1
 Zheng, Z., Tinker, J. L., Weinberg, D. H., & Berlind, A. A. 2002, ApJ, 575, 617
 Zheng, Z. 2004, ApJ, 610, 61
 Zheng, Z., Berlind, A. A., Weinberg, D. H., Benson, A. J., Baugh, C. M., Cole, S., Davé, R., Frenk, C. S., Katz, A., & Lacey, C. G. 2005, ApJ, 633, 791
 Zheng, Z. & Weinberg, D. H. 2005, ApJ, submitted (astro-ph/0512071)
 Zhu, G., Zheng, Z., Lin, W. P., Jing, Y. P., Kang, X., & Gao, L. 2006, ApJ, 639, L5